Contemporary tectonic deformation of the Basin and Range province, western United States: 10 years of observation with the Global Positioning System

William C. Hammond[1] and Wayne Thatcher
Earthquake Hazards Team, U.S. Geological Survey, Menlo Park, California, USA

Received 19 August 2003; revised 16 March 2004; accepted 11 May 2004; published 5 August 2004.

[1] We have estimated patterns and rates of crustal movement across 800 km of the Basin and Range at ~39° north latitude with Global Positioning System surveys in 1992, 1996, 1998, and 2002. The total rate of motion tangent to the small circle around the Pacific-North America pole of rotation is 10.4 ± 1.0 mm/yr, and motion normal to this small circle is 3.9 ± 0.9 mm/yr compared to the east end of our network. On the Colorado Plateau the east end of our network moves by ~1–2 mm/yr westerly with respect to North America. Transitions in strain rates delimit six major tectonic domains within the province. These deformation zones coincide with areas of modern seismicity and are, from east to west, (1) east-west extension in the Wasatch Fault zone, (2) low rate east-west extension centered near the Nevada-Utah border, (3) low rate east-west contraction between 114.7°W and 117.9°W, (4) extension normal to and strike-slip motion across the N10°E striking Central Nevada Seismic Zone, (5) right lateral simple shear oriented N13°W inside the Walker Lane Belt, and (6) shear plus extension near the Sierra Nevada frontal faults. Concentration of shear and dilatational deformation across the three westernmost zones suggests that the Walker Lane Belt lithosphere is rheologically weak. However, we show that linear gradients in viscosity and gravitational potential energy can also effectively concentrate deformation. In the Basin and Range, gradients in gravitational potential are spatially anticorrelated with dilatational strain rates, consistent with the presence of horizontal variations in viscosity of the lithosphere. *INDEX TERMS:* 1208 Geodesy and Gravity: Crustal movements—intraplate (8110); 8109 Tectonophysics: Continental tectonics—extensional (0905); 8122 Tectonophysics: Dynamics, gravity and tectonics; 8150 Tectonophysics: Plate boundary—general (3040); 8159 Tectonophysics: Rheology—crust and lithosphere; *KEYWORDS:* Basin and Range, global positioning system, tectonic deformation, extension, plate boundary

Citation: Hammond, W. C., and W. Thatcher (2004), Contemporary tectonic deformation of the Basin and Range province, western United States: 10 years of observation with the Global Positioning System, *J. Geophys. Res.*, *109*, B08403, doi:10.1029/2003JB002746.

1. Introduction

[2] The Basin and Range province of the western United States typifies active continental extension and is one of the Earth's most studied regions of distributed continental deformation. The province-wide extensional history has been investigated by many authors (e.g., see reviews by *Parsons* [1995] and *Sonder and Jones* [1999]). They describe rates of extension that vary substantially in time and space, between 4 and 20 mm/yr over the last 35–45 Myr. The later stages of this extension made the pattern of alternating ranges and valleys that is characteristic of the province [*Zoback et al.*, 1981]. Modern survey techniques, including space geodesy, have the sensitivity to detect motions of this magnitude over a few years' time and thus can be used to address how the Basin and Range is deforming today.

[3] Previous studies used space geodesy measured deformation across the Basin and Range province. *Minster and Jordan* [1984, 1987] inferred a west-northwest extension direction using Very Long Baseline Interferometry (VLBI) and geological observations. VLBI and satellite laser ranging were used to identify an Euler pole of rotation for the Sierra Nevada–Great Valley microplate (SNGV) [*Argus and Gordon*, 1991] and to infer concentrations of the deformation near the Wasatch Fault Zone (WFZ) and the westernmost Basin and Range [*Dixon et al.*, 1995]. Surveys using the Global Positioning System (GPS) [e.g., *Bennett et al.*, 1998; *Thatcher et al.*, 1999] also indicated that crustal deformation is strongly concentrated in the western 200 km of the Basin and Range and across the WFZ at the eastern boundary of the province. *Thatcher et al.* [1999] measured

[1]Now at Nevada Bureau of Mines and Geology, University of Nevada, Reno, Reno, Nevada, USA.

about 10 mm/yr of relative motion between the Central Nevada Seismic Zone (CNSZ) at longitude 118°W and the SNGV at longitude 120°W, while an additional ~3 mm/yr of motion occurs across the WFZ in central Utah. *Svarc et al.* [2002] focused GPS observation on western Nevada and characterized the deformation with a horizontal tensor strain rate analysis. Within the CNSZ they found a combination of right lateral simple shear with a component of extension normal to the strike of the range-bounding faults, consistent with trilateration results of *Savage et al.* [1995]. The westernmost subarray of *Svarc et al.* [2002] abuts the SNGV, where they found a strain rate field with an extensional axis that is near east-west, consistent with a change in regional fault strike near the Sierra Nevada frontal fault zone.

[4] Here we investigate the contemporary motions of the Basin and Range province over the time span of one decade (1992–2002). We estimate the horizontal tensor strain rate using previously and newly collected campaign GPS data from a geodetic network that spans the entire Basin and Range province at 39° north latitude. Compared to the earlier analysis of 1992–1998 data by *Thatcher et al.* [1999], we have a greater number of sites and greater certainty in site velocities. Surveying sites off the main axis of the network (to the north and south) allows us to constrain the deformation style and orientation along our predominantly east-west network for the first time. The relatively long record of GPS observations gives us improved resolution in site velocities and forms the basis for the strain rate analysis presented here. The GPS results show a strong relationship between Holocene faulting and contemporary deformation, suggesting that motions measured by GPS can be used to infer deformation over many earthquake cycles. Finally, we place new constraints on Basin and Range dynamics by considering the relation between the GPS-observed deformation and the forces inferred from gravitational potential energy estimated from the geoid.

2. Data Collection and Analysis

[5] Our network (Figure 1) consists of 90 geodetic benchmarks surveyed in 1992, 1996, 1998, and 2002. The network spans the entire province near 39° north latitude, extending from east of the Wasatch Fault Zone in Utah (longitude ~111°W) to west of the Sierra Nevada frontal fault zone and Lake Tahoe (longitude ~120°W) in the northern Sierra Nevada of California, primarily along Interstate Highway 50. The network is identical to that described by *Thatcher et al.* [1999], except that 23 additional sites were added in 1998 to increase the spatial density of sampling. Its orientation is roughly normal to the strike of the major range-bounding normal faults that form the topography characteristic of the Basin and Range. This study utilizes all of the data from *Thatcher et al.* [1999] as well as data from the survey carried out in September 2002.

[6] Each site was visited multiple times, with at least 4 years and at most 10 years between the first and most recent occupation. Fifty-five of 90 sites have 10 years of occupation history (Table 1). Sites on the central axis of the network (Figure 1) were generally observed twice for at least 6.5 hours per campaign, while the off-axis sites north and south of the main axis of the network were designed to collect data while unattended and were generally occupied for between two and five 24-hour sessions per campaign. In 1998, when the 23 new sites were installed, only one 6.5-hour day of data was collected at these sites. Velocities from these sites are not presented here because of their larger uncertainties but were included in the processing to aid in the resolution of integer wavelength carrier phase ambiguities, thereby improving position precision at the other sites. In a few cases, monuments were destroyed between surveys, requiring replacement at a nearby location. In these cases, two nearby sites were analyzed as a single site during the network adjustment step (described below), providing one estimate for site velocity (Table 1).

[7] The daily positions of the stations were obtained by reducing the data with the GIPSY/OASIS II software [*Webb and Zumberge*, 1995], using the point-positioning method [*Zumberge et al.*, 1997] and final satellite and clock files from the Jet Propulsion Laboratory. Following point positioning, carrier phase ambiguities were estimated inside small, overlapping subsets of the stations, which reduced uncertainty in the results. This procedure determines site coordinates that are effectively in a reference frame defined by the orbits of the satellites. We transformed these coordinates into a North America reference frame (Appendix A). Because the realization of North America varies slightly from one study to the next, we also present our velocities in the International Terrestrial Reference Frame 2000 (ITRF2000) (Table 1).

[8] Once daily positions are obtained, constant velocities are estimated for each site through linear regression, and a subsequent network adjustment for daily uncertainty in the reference frame. We use the Quasi-Observation Combination Analysis (QOCA) [*Dong et al.*, 1998] software to perform this adjustment, which uses a Kalman filter approach to apply a daily reference frame transformation (seven total Helmert parameters for translation, rotation, and scale). Such a transformation insures that the inferred motions of all sites are as consistent as possible with velocities that are constant in time. In this adjustment, solutions for 51 International GPS Service (IGS) global tracking stations and a subset of the nearest continuously recording stations in the Basin and Range Geodetic Network (BARGEN) [*Bennett et al.*, 1998] (COON, DYER, ECHO, EGAN, ELKO, GABB, GARL, GOSH, HEBE, MINE, SHIN, SHOS, SLID, SMEL, TONO, TUNG, UPSA) and the site QUIN were included. Obvious outliers in the time series are identified and removed before performing the QOCA adjustment in the global mode.

[9] Formal estimates of uncertainty are obtained in a four-step procedure. This method preserves the relative magnitude of uncertainties for sites with different lengths and frequency in occupation history, and varying uncertainty in individual daily positions. In the first step the GIPSY-OASIS II software formally estimates uncertainties in the positions. These are usually deemed to be too small since they are smaller than the repeatabilities obtained from continuous GPS sites. The underestimate of coordinate uncertainty manifests itself during the adjustment step using the QOCA software and gives incremental χ^2 per degrees of freedom ($\delta\chi^2$) that are too large. In the second step we estimate site velocity by reweighting the uncertainty in daily site positions by a scale factor of 2.0 for the east and north

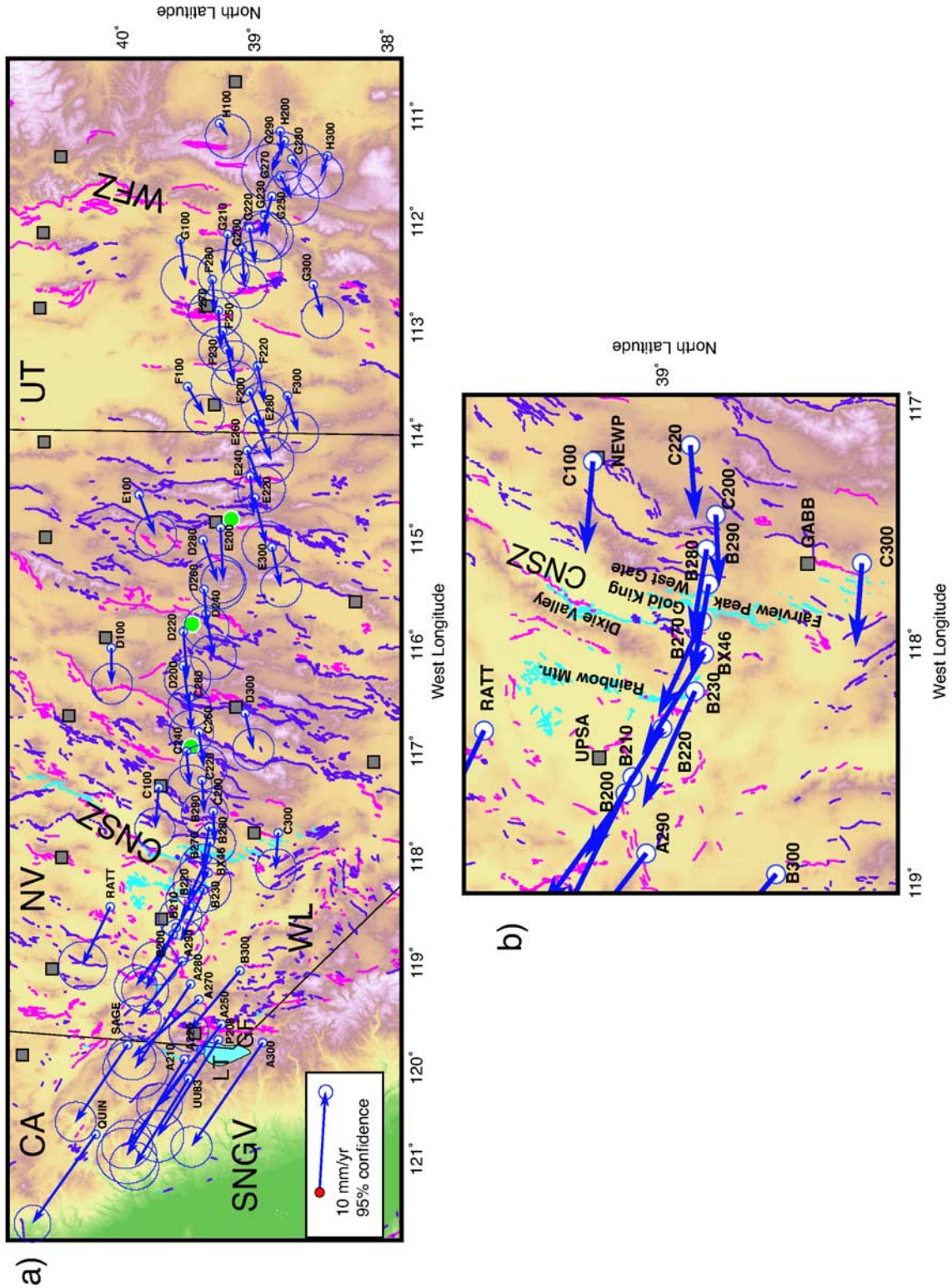
a)
b)
North Latitude
West Longitude
CA
NV
UT
WL
SNGV
CNSZ
WFZ
LT
GT
10 mm/yr
95% confidence
RATT
SAGE
QUIN
UU83
UPSA
NEWP
GABB
Dixie Valley
Gold King
West Gate
Fairview Peak
Rainbow Mtn.

Figure 1

components. This results in uncertainties in velocity that are slightly greater than estimates made without the scale factor. In the third step we add a contribution from time-correlated, or "colored," noise that exists in crustal strain data [*Agnew*, 1992]. To estimate the total uncertainty σ, we add to the formal white noise uncertainty in velocity σ_{WN} an uncorrelated component of random walk noise σ_{RW} [*Langbein and Johnson*, 1997]:

$$\sigma = \sqrt{\sigma_{WN}^2 + \sigma_{RW}^2}, \qquad \sigma_{RW} = \frac{a}{\sqrt{t}}, \tag{1}$$

where t is the time interval between the first and last survey in years and a is assumed to be 1 mm/yr$^{1/2}$. Recent studies suggest that white noise plus flicker noise is a more accurate noise model than the white noise plus random walk model that we use [*Williams et al.*, 2004]. However, in the final step the uncertainties in the data are adjusted so that the intrinsic variation of the velocities matches their uncertainty. The result is that we find the uncertainties obtained in steps 1–3 to be too large, and hence our error estimation was too conservative.

[10] We estimate the intrinsic variation of the velocity by finding the best fitting constant strain rate tensor inside subgroups of 10–12 sites (see section 4) and subtracting the velocity prediction made by this estimated constant strain rate from the observed velocity. The misfit is summarized by

$$\chi^2 = \frac{1}{2N - M}(d - Gm)^T C_d^{-1}(d - Gm), \tag{2}$$

where N is the number of GPS sites, $M = 6$ is the number of parameters estimated in the inversion for the horizontal strain rate tensor (three rigid rotation and three strain rate parameters), d is a vector of velocities, C_d is the diagonal covariance matrix containing the variances of velocity estimates, Gm is the velocity predicted from the constant strain rate tensor, and T denotes the matrix transpose. If we assume that all variation in the velocities unexplained by a constant strain rate originates from uncertainty in our velocity estimates, then the standard deviation of the residual velocity provides an empirical estimate for the velocity uncertainty. Any real variation in strain rate unaccounted for by the constant strain rate model would increase this empirical estimate of uncertainty. Thus the empirical estimate is an upper bound on the true uncertainty in the velocity estimate. In eastern Nevada, where little or no significant deformation is observed (between longitude 117°W and 112°W), the mean $\chi^2 = 0.2$, so we scale the velocity uncertainties by $(0.2)^{1/2} = 0.44$. The relative contributions from each of the above mentioned sources of uncertainty are listed in Table 2. The resulting mean uncertainty in east and north velocity is ~0.4 mm/yr. However, because the strain rate is derived from the relative velocity between sites, most of the reference frame uncertainty has been removed by applying this scaling. For that reason, we use the smaller uncertainties obtained from steps 1–4 above in the calculations of the strain rate tensors but use the larger uncertainties obtained from steps 1–3 when presenting velocities with respect to North America (Figure 2a and Table 1).

[11] Throughout this paper, quoted uncertainties in the text are one standard deviation, while figures with error bars or error ellipses show two standard deviations. Azimuths are geographic and count degrees clockwise from north when viewed from a point above the Earth, unless specified otherwise. Strain rates are provided in nanostrain (nstr) per year, and rotations are provided in nanoradians (nrads) per year.

3. Velocities

[12] Almost all of the variation in site velocity with respect to North America is in the westernmost ~200 km (west of 117.7°W) and easternmost ~50 km (east of 112°W) of the Basin and Range. The easternmost zone is near the WFZ, where east velocity changes from approximately −4 mm/yr to near −1 mm/yr. The north velocity varies only weakly east of 117.7°W. West of 117.7°W, the east and north velocities begin to increase steadily through 120°W, where the velocities become close to those of the Sierra Nevada microplate (SNGV) (e.g., QUIN and A300 in Figures 2a–2f).

[13] Our results are generally in good agreement with the velocities presented by *Thatcher et al.* [1999]. A slight disruption in the pattern of the velocities near 119°W is visible in both the east and north velocity components. This feature, along with a slightly elevated velocity for one station, was interpreted by *Thatcher et al.* [1999] as a consequence of motion on a west dipping fault near the CNSZ, in combination with motion on an east dipping fault near the Genoa fault. Our results do not show the elevated velocity at longitude 118°W, where a local maximum was predicted by their dipping fault model. Also not present in our results is the elevated velocity of the site near 112°W, just east of the WFZ observed by *Thatcher et al.* [1999]. Compared to *Thatcher et al.* [1999], our velocities are consistently more southerly, indicating a difference in velocity reference frame of ~1–2 mm/yr. Reference frame issues are discussed more completely below.

Figure 1. (a) GPS velocity across the Basin and Range, western United States with respect to North America (blue vectors) with 95% confidence ellipses superimposed on topography (Lambert conic projection). Confidence ellipses include uncertainty in the North America reference frame. (b) Expanded view of faults around the Central Nevada Seismic Zone. Faulting is shown with colored lines: cyan (historic), magenta (Holocene), and purple (Late Quaternary). Nearby BARGEN sites are shown with gray squares. Abbreviations are as follows: SNGV, Sierra Nevada–Great Valley microplate; CA, California; NV, Nevada; UT, Utah; CNSZ, Central Nevada Seismic Zone; GF, Genoa Fault; LT, Lake Tahoe; WFZ, Wasatch Fault Zone; WL, Walker Lane Belt. Green circles from west to east are the towns of Austin, Eureka, and Ely.

Table 1. Station Coordinates, Observation Histories, and Velocities

					ITRF2000		NA		σ_{NA}[c]		σ_{NET}[d]	
Station	Latitude	Longitude	Days[a]	Years[b]	V_N	V_E	V_N	V_E	σ_N	σ_E	σ_N	σ_E
A210	39.358	−120.142	4	6.0	−7.3	−22.6	5.6	−10.2	1.26	1.16	0.55	0.51
A220	39.238	−120.033	4	9.9	−5.3	−22.8	7.6	−10.5	1.07	1.03	0.47	0.45
A250	39.102	−119.774	8	10.0	−6.7	−21.0	6.1	−8.6	0.96	0.92	0.42	0.40
A270	39.282	−119.550	5	10.0	−6.9	−19.3	5.9	−6.9	0.99	0.92	0.44	0.40
A275[e]	39.348	−119.412	3	10.0	−7.7	−21.3	5.1	−8.9	1.37	1.23	0.60	0.54
A280[e]	39.350	−119.406	2	4.0	−7.7	−21.3	5.1	−8.9	1.37	1.23	0.60	0.54
A281[e]	39.350	−119.406	3	2.0	−7.7	−21.3	5.1	−8.9	1.37	1.23	0.60	0.54
A290	39.429	−119.194	6	9.9	−8.3	−18.5	4.3	−6.0	0.94	0.90	0.41	0.40
A300	38.777	−119.924	10	10.0	−6.1	−23.3	6.8	−11.1	0.86	0.85	0.38	0.37
B100[f]	39.995	−118.703	3	10.0	−9.9	−18.8	2.6	−6.2	1.01	1.00	0.44	0.44
B200	39.513	−118.939	14	9.9	−9.0	−17.9	3.6	−5.3	0.89	0.86	0.39	0.38
B210	39.493	−118.867	6	9.9	−10.3	−19.2	2.2	−6.7	0.98	0.95	0.43	0.42
B220	39.398	−118.646	6	10.0	−9.0	−18.5	3.5	−5.9	0.95	0.92	0.42	0.40
B230	39.299	−118.472	7	9.9	−10.6	−18.0	1.8	−5.4	0.94	0.91	0.41	0.40
B270	39.286	−118.173	7	10.0	−10.3	−16.9	2.1	−4.3	0.93	0.90	0.41	0.40
B280	39.275	−118.017	5	6.0	−11.7	−16.8	0.6	−4.2	1.22	1.17	0.54	0.51
B290	39.284	−117.859	7	10.0	−11.2	−16.6	1.1	−3.9	0.96	0.93	0.42	0.41
B300	38.988	−119.244	24	9.9	−7.7	−18.9	4.9	−6.5	0.82	0.83	0.36	0.37
BX46	39.274	−118.311	11	10.0	−9.8	−17.3	2.6	−4.7	0.90	0.88	0.40	0.39
C100	39.686	−117.509	13	9.9	−11.9	−16.9	0.2	−4.1	0.84	0.84	0.37	0.37
C200	39.264	−117.712	14	9.9	−12.4	−15.9	−0.3	−3.3	0.88	0.86	0.39	0.38
C220	39.358	−117.412	6	9.9	−12.3	−16.1	−0.2	−3.4	0.97	0.93	0.43	0.41
C240	39.487	−117.142	7	9.7	−12.4	−16.3	−0.4	−3.5	0.93	0.89	0.41	0.39
C260	39.402	−116.942	7	9.9	−12.3	−16.4	−0.3	−3.6	0.99	0.94	0.44	0.41
C280	39.477	−116.621	7	10.0	−11.9	−16.3	0.0	−3.4	0.93	0.90	0.41	0.40
C300	38.760	−117.884	14	9.6	−12.1	−16.2	0.1	−3.7	0.85	0.86	0.37	0.38
D100	40.084	−116.161	12	9.7	−11.8	−16.7	−0.1	−3.6	0.86	0.85	0.38	0.37
D200	39.534	−116.306	14	9.9	−12.4	−17.1	−0.7	−4.2	0.90	0.88	0.40	0.39
D220	39.543	−115.976	7	9.9	−12.4	−17.8	−0.7	−4.8	0.97	0.93	0.43	0.41
D240	39.381	−115.799	7	9.9	−12.7	−17.3	−1.1	−4.4	0.96	0.94	0.42	0.41
D260	39.402	−115.556	7	9.9	−11.9	−16.9	−0.4	−3.9	0.95	0.91	0.42	0.40
D280	39.415	−115.082	6	6.0	−13.1	−17.3	−1.7	−4.3	1.18	1.14	0.52	0.50
D300	39.056	−116.746	22	9.7	−12.8	−16.5	−0.9	−3.7	0.87	0.87	0.38	0.38
E100	39.902	−114.652	13	9.9	−13.2	−17.4	−1.9	−4.2	0.88	0.88	0.39	0.39
E200	39.290	−114.954	14	9.9	−11.7	−18.2	−0.4	−5.2	0.91	0.90	0.40	0.40
E220	39.033	−114.658	7	9.9	−12.3	−17.6	−1.1	−4.6	1.00	0.99	0.44	0.44
E240	39.069	−114.454	7	9.9	−11.4	−16.8	−0.2	−3.8	0.96	0.98	0.42	0.43
E260	39.097	−114.204	5	9.9	−12.7	−16.7	−1.6	−3.7	1.00	0.98	0.44	0.43
E280	39.045	−113.887	7	9.9	−12.6	−17.2	−1.6	−4.1	0.95	0.97	0.42	0.43
E300	38.890	−115.130	14	9.9	−12.3	−16.9	−0.9	−4.0	0.86	0.85	0.38	0.37
F100	39.549	−113.585	12	9.9	−12.4	−16.0	−1.5	−2.7	0.84	0.84	0.37	0.37
F200	39.081	−113.630	8	9.9	−12.2	−17.1	−1.3	−4.0	0.92	0.90	0.40	0.40
F220	39.024	−113.385	5	9.9	−11.4	−16.9	−0.6	−3.7	0.96	0.92	0.42	0.40
F230	39.254	−113.224	5	9.9	−11.5	−16.5	−0.7	−3.3	0.97	0.92	0.43	0.40
F250	39.283	−113.046	7	9.9	−11.8	−16.4	−1.1	−3.1	0.94	0.91	0.41	0.40
F270	39.317	−112.837	5	9.9	−10.8	−17.2	−0.2	−3.9	0.95	0.91	0.42	0.40
F280	39.367	−112.546	5	9.9	−10.7	−16.7	−0.2	−3.4	1.10	1.00	0.48	0.44
F300	38.795	−113.667	12	9.9	−11.8	−16.6	−0.9	−3.6	0.85	0.85	0.37	0.37
G100[g]	39.601	−112.148	4	3.9	−10.3	−17.3	0.1	−3.8	1.04	1.05	0.46	0.46
G101[g]	39.602	−112.151	5	4.0	−10.3	−17.3	0.1	−3.8	1.04	1.05	0.46	0.46
G200	39.140	−112.242	10	9.9	−10.7	−17.1	−0.2	−3.8	0.96	0.92	0.42	0.40
G210	39.241	−112.098	5	9.9	−9.2	−17.3	1.2	−3.9	1.08	1.02	0.48	0.45
G220	39.078	−112.042	5	9.9	−10.4	−16.8	0.0	−3.5	1.09	1.00	0.48	0.44
G230	38.961	−111.915	5	9.9	−9.7	−15.3	0.7	−2.0	1.09	1.01	0.48	0.44
G250	38.904	−111.738	7	9.9	−8.5	−17.3	1.8	−3.9	1.10	1.08	0.48	0.48
G270	38.839	−111.537	5	9.9	−10.3	−15.0	−0.1	−1.7	1.14	1.12	0.50	0.49
G280	38.755	−111.381	5	9.9	−10.2	−14.2	0.0	−0.9	1.13	1.08	0.50	0.48
G290	38.808	−111.206	4	6.0	−8.8	−16.5	1.4	−3.1	1.23	1.19	0.54	0.52
G300	38.602	−112.594	12	9.9	−11.2	−16.4	−0.6	−3.2	0.88	0.87	0.39	0.38
H100	39.293	−111.020	9	9.9	−10.6	−14.7	−0.6	−1.3	0.94	0.93	0.41	0.41
H200	38.833	−111.111	7	9.9	−9.5	−15.7	0.6	−2.3	1.07	1.02	0.47	0.45
H300	38.483	−111.359	7	9.9	−8.9	−15.2	1.2	−1.9	0.94	0.93	0.41	0.41
P208	39.111	−119.923	10	7.0	−7.2	−22.8	5.7	−10.4	1.09	1.08	0.48	0.48

Table 1. (continued)

Station	Latitude	Longitude	Days[a]	Years[b]	ITRF2000 V_N	ITRF2000 V_E	NA V_N	NA V_E	σ_{NA}[c] σ_N	σ_{NA}[c] σ_E	σ_{NET}[d] σ_N	σ_{NET}[d] σ_E
QUIN	39.975	−120.944	245	9.7	−7.3	−22.1	5.9	−9.7	0.77	0.77	0.34	0.34
RATT[f]	39.995	−118.703	14	6.0	−9.9	−18.8	2.6	−6.2	1.01	1.00	0.44	0.44
SAGE	39.791	−120.039	16	10.0	−7.9	−20.7	5.0	−8.2	0.85	0.84	0.37	0.37
UU83	39.318	−120.325	14	7.0	−8.2	−21.7	4.8	−9.4	1.02	1.00	0.45	0.44

[a]Total number of days of data collected.
[b]Time span between first and most recent observation.
[c]σ_{NA} is uncertainty of velocity with respect to nondeforming North America.
[d]$\sigma_{NET} = 0.44\sigma_{NA}$, approximates uncertainty with respect to other sites in the network.
[e]A275, A280, and A281 were tied together.
[f]B100 and RATT were tied together.
[g]G100 and G101 were tied together.

[14] Motion parallel and normal to Pacific–North America (PA/NA) relative motion suggests the presence of dextral shear strain in the westernmost 200 km of our network, with a domain of nearly uniaxial extension near the WFZ. These velocities are plotted as a function of distance from the PA/NA pole in Figures 2d and 2e. At every site we define the relative plate motion normal component of velocity $v_\perp$ as that which lies along the great circle connecting the site and the PA/NA pole of rotation of *Argus and Gordon* [2001] (75.9°W, 50.1°N), positive in the direction ∼N125°W. The relative plate motion parallel velocity $v_{//}$ is the horizontal component perpendicular to $v_\perp$ (positive in the direction ∼N35°W). West of longitude 117.7°W (∼−100 km plate boundary normal distance), $v_{//}$ increases from ∼1 mm/yr to ∼12 mm/yr. Since these velocities are parallel to the nominally transform motion of the Pacific plate with respect to the North American plate, they suggest that this deformation results from shear tractions applied by motion of the Pacific plate past the SNGV.

[15] The azimuth of GPS velocity changes abruptly near 118°W longitude, indicating that the CNSZ is a fundamental transition in the character of Basin and Range motion (Figures 1 and 2). The uncertainty in azimuth is larger when the east and north components become smaller in the eastern Basin and Range. However, the velocities are sufficiently well determined to show that the azimuth changes by ∼35° to 40° at 118°W (at −160 km in Figure 2f).

[16] Velocities on the easternmost end of the network near the WFZ approach but do not quite achieve zero velocity with respect to our realization of stable North America. A small amount of apparent motion is observed at the easternmost end of the network, near longitude 111°W (Figures 2a and 2d). The east velocity is above the level of significance at 95% confidence for the three easternmost sites, G290, H100, and H200 (−3.1 ± 0.4, −2.6 ± 0.4, and −1.4 ± 0.4, respectively). *Bennett et al.* [2003] report significant positive western velocities of 2.02 ± 0.07, 0.35 ± 0.07, and 2.92 ± 0.08 mm/yr, respectively, for the three closest and easternmost continuously operating BARGEN sites (COON, HEBE, and SMEL). Solving for the solid body rotation rate that best explains the difference between our results and theirs (Appendix A) yields a velocity of ∼1.6 mm/yr oriented roughly north. Hence both studies agree that some westward motion exists near the eastern end of our network but disagree (by ∼1.6 mm/yr) on how much north directed motion exists. That is, both studies imply that some deformation occurs between 111°W longitude and the interior of the nondeforming North American plate to the east, perhaps associated with opening of the Rio Grande Rift at the eastern boundary of the Colorado Plateau.

4. Strain Rates

[17] To estimate tensor strain rate, we use the method of *Savage et al.* [2001, equation (A6)] to obtain the average strain rate tensor in spherical coordinates at the centroid of a network. This method estimates the spatial derivates of velocity to find the best fitting horizontal tensor strain rates and rigid rotations around the Earth center. Thus our estimates of strain rate are not dependent on the reference frame, which affects only rigid motion of the entire network. Variations in slope in the velocity profiles (Figure 2) indicate that a uniform estimate of strain rate for our entire network will not be appropriate, so we have estimated strain rates for many subnetworks to identify transitions in the style and rate of deformation. We apply a moving window from west to east centered on the network-bisecting path, selecting the 10 GPS sites nearest the center. Occasionally, we add an additional site or two to assure that there is sufficient representation of off-axis sites. Each subnetwork has a nearly equal areal footprint size since our network site density is roughly uniform in the east-west direction. For each subnetwork

Table 2. Mean Uncertainties in Velocities With Respect to North America[a]

	σ_{VNorth}	σ_{VEast}
Without Random Walk		
GIPSY Formal Errors	0.71	0.88
GIPSY + QOCA	0.89	0.86
With Random Walk Included, a = 1 mm/sqrt (yr)		
GIPSY Formal Errors	0.79	0.94
GIPSY + QOCA	0.99	0.96
With Random Walk, Scaled So $\chi^2 = 1.0$		
GIPSY + QOCA	0.44	0.42

[a]Mean uncertainties are in mm/yr.

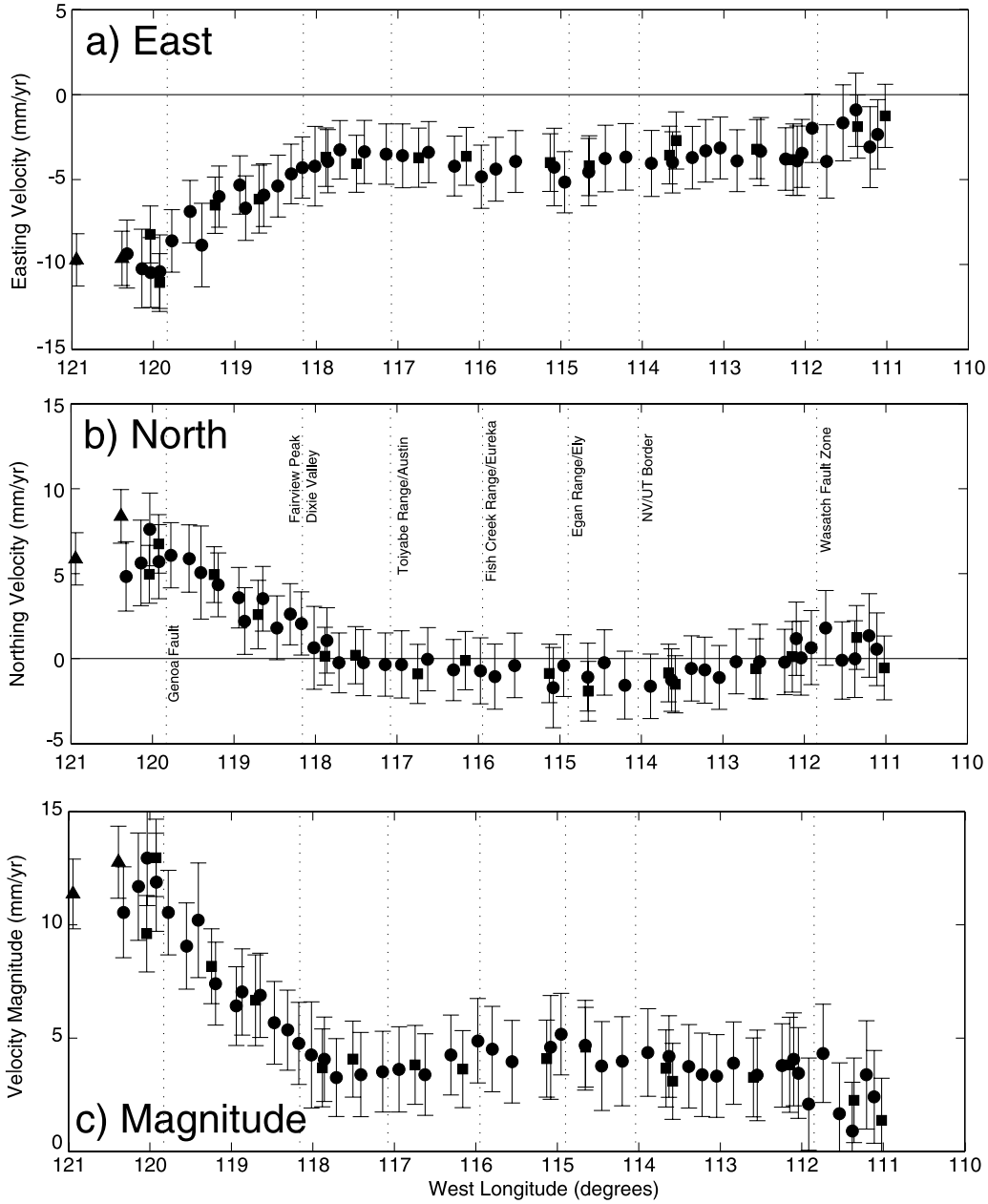

Figure 2. (a) East component, (b) north component, and (c) magnitude of velocity with respect to North America. The error bars indicate 2σ uncertainty. Vertical dotted lines show longitude of the indicated fault or geographic feature, squares are off-axis sites, circles are on-axis sites, and triangles are the sites QUIN (near 121°W) and CMBB (near 120.5°W) on the SNGV. (d) Relative plate motion normal component $V_{\perp}$, i.e., component of GPS velocity that lies along the great circle between the Pacific–North America pole of rotation and the GPS site, positive to the northeast, (e) relative plate motion parallel component $V_{//}$, i.e., the horizontal component tangent to the small circle around the pole, positive northwest, and (f) geographic azimuth of velocity, measured as degrees clockwise from north. Horizontal axis is distance from the center of the network projected along the great circle connecting the Pacific–North America pole and the center of the network. Other symbols are as in the previous figure.

the maximum and minimum principal strain rates (ε_1 and ε_2), maximum shear strain rate $\gamma/2$, dilatation ε_Δ, and rotation rate ω are estimated, along with their formal uncertainties (Figure 3). Subnetworks overlap so the spatial variation in strain rate has been smoothed. The purpose of this representation of the deformation field is to identify where transitions in the magnitude and style of the deformation field occur and to aid in selection of subnetworks for more detailed analysis. The maximum shear strain rate $\gamma/2 = (\varepsilon_1 - \varepsilon_2)/2$ is the smaller principal strain subtracted from the larger, so the distribution of $\gamma/2$ is not Gaussian. Thus $\gamma/2$ is likely not significantly

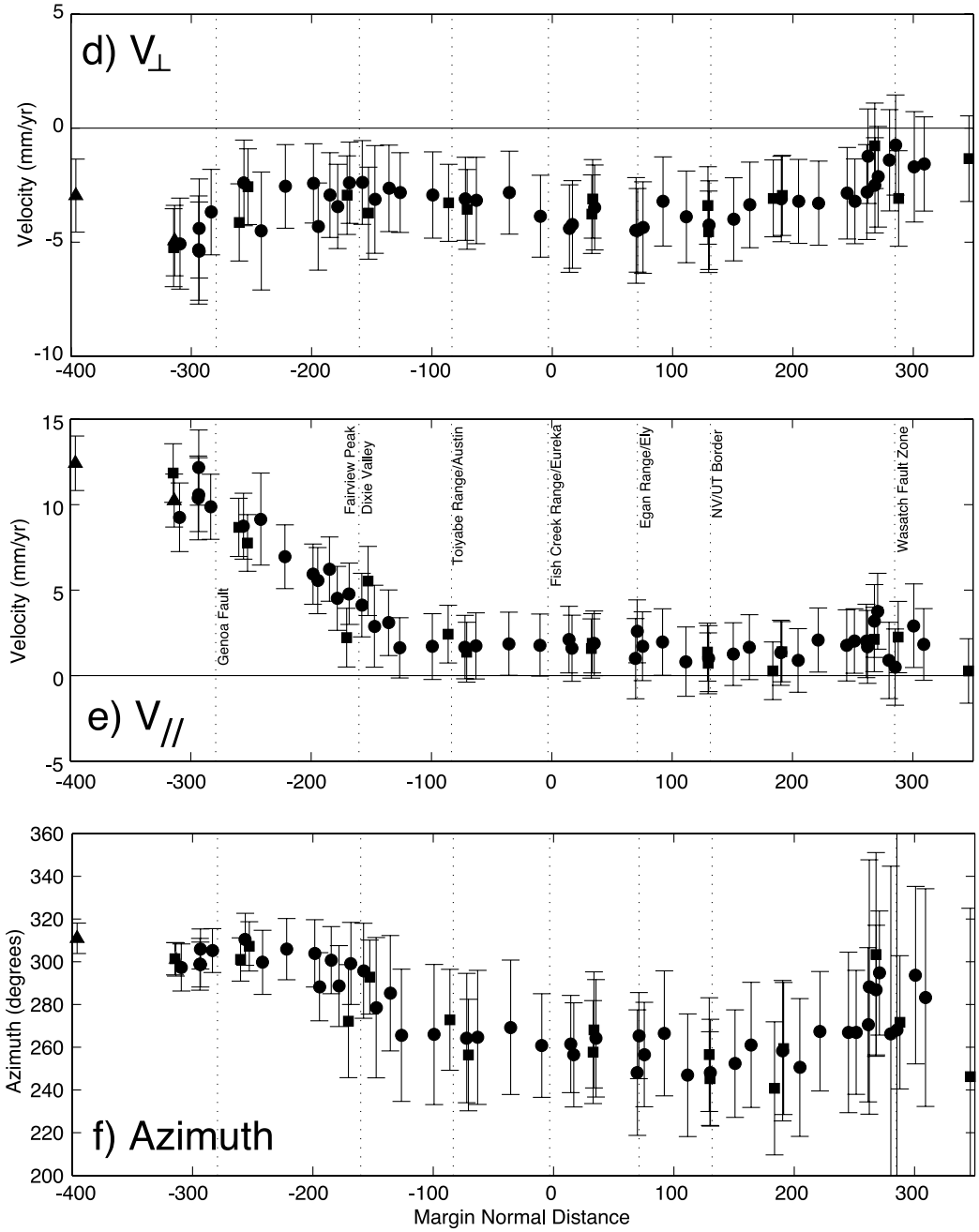

Figure 2. (continued)

different than zero between 117.7°W and 112°W longitude (Figure 4).

4.1. Nevada

[18] Most of the deformation of our network occurs west of 117.7°W longitude, where there is significant dextral shear and dilatation (Figure 4). The rotation rates are opposite in sign and about equal in magnitude to the maximum shear rate, indicating right lateral simple shear. Extension is significant, consistent with the findings of *Svarc et al* [2002], who used 1992–2000 data from our sites west of site B290 plus 22 additional sites north and south of our network. Dilatation $\varepsilon_\Delta \equiv \varepsilon_1 + \varepsilon_2$ is positive, averaging ~20 nstr/yr. The high strain rates west of 117.5°W can be divided into three subdomains, each having a distinguishable style of deformation. Figure 5 and Table 3 show the strain rate estimates inside three nonoverlapping subnetworks west of 117.7°W and four nonoverlapping subsets east of 117.7°W.

[19] In the vicinity of the CNSZ, crustal deformation can be characterized as having a largely uniaxial extension oriented N53.0 ± 2.2°W. For the seven sites between longitude 117.7°W and 118.3°W (Group 3 of Table 3), ε_1 = 44.5 ± 9.7 and ε_2 = −11.5 ± 8.8 nstr/yr. Including additional sites straddling the CNSZ (Group CNSZ of Table 3) results in the same apparently uniaxial character

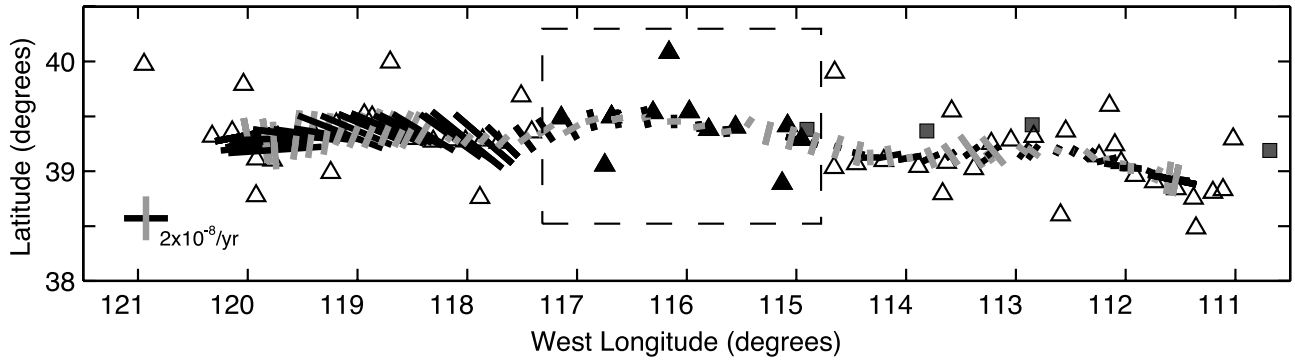

Figure 3. Tensor strain rates estimated from GPS velocity across the Basin and Range projected onto map view of our network. Triangles indicate position of GPS sites; black solid triangles outlined with dashed box are one sample subnetwork illustrating the spatial smoothing length scale. At the centroid of each subnetwork, black bars indicate direction and magnitude of maximum principal extension. Gray bars indicate contraction. Gray squares are locations of the BARGEN sites (from west to east) EGAN, FOOT, SMEL, and CAST referenced in the text.

to the deformation ($\varepsilon_1 = 34.6 \pm 3.8$, $\varepsilon_2 = -6.2 \pm 4.5$ nstr/yr). Adding the site RATT, however, introduces a small but significant increase in the magnitude of ε_2, resulting in significant shear across a larger zone centered on the CNSZ ($\varepsilon_1 = 31.7 \pm 3.3$, $\varepsilon_2 = -8.3 \pm 3.8$). It is possible that RATT, the westernmost site in the group, is measuring some of the simple shear associated with the interior of the WL. We determine the extensional strain rate normal to

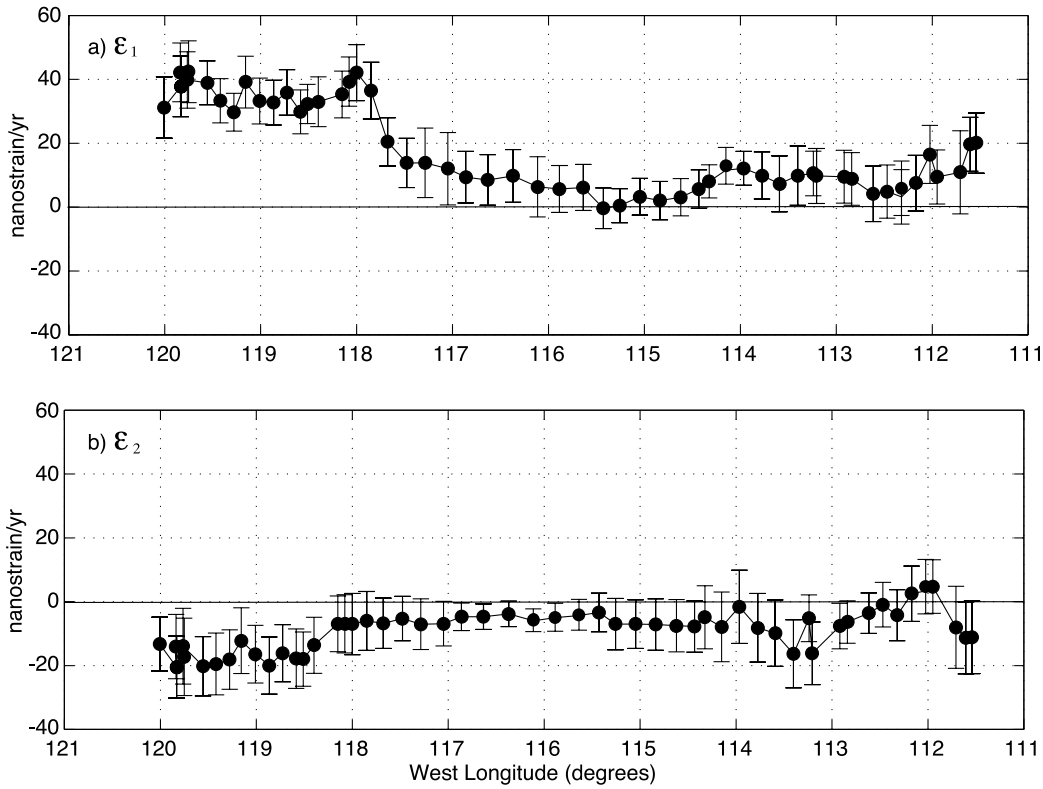

Figure 4. (a) Maximum principal strain rate obtained from subsets of 10–12 GPS sites applied across the network. (b) Minimum principal strain rate. Error bars are 2σ uncertainty. (c) Dilatational component of strain rate (area change) for each of the subgroups, (d) maximum shear strain rate, and (e) rotation rate. Error bars are 2σ model uncertainty. In Figure 4d, errors are likely not Gaussian near $\gamma/2 = 0$; hence the gray region has been added to show approximate threshold of resolvability. Rotation rate is positive when the network rotates counterclockwise when viewed from above the surface of the Earth. (f) Geographic azimuth of direction of maximum extension, measured in degrees from north, counterclockwise reckoned positive. Error bars are 2σ uncertainty. (g) χ^2 misfit between measured velocity and that predicted by the strain rate estimate according to equation (2).

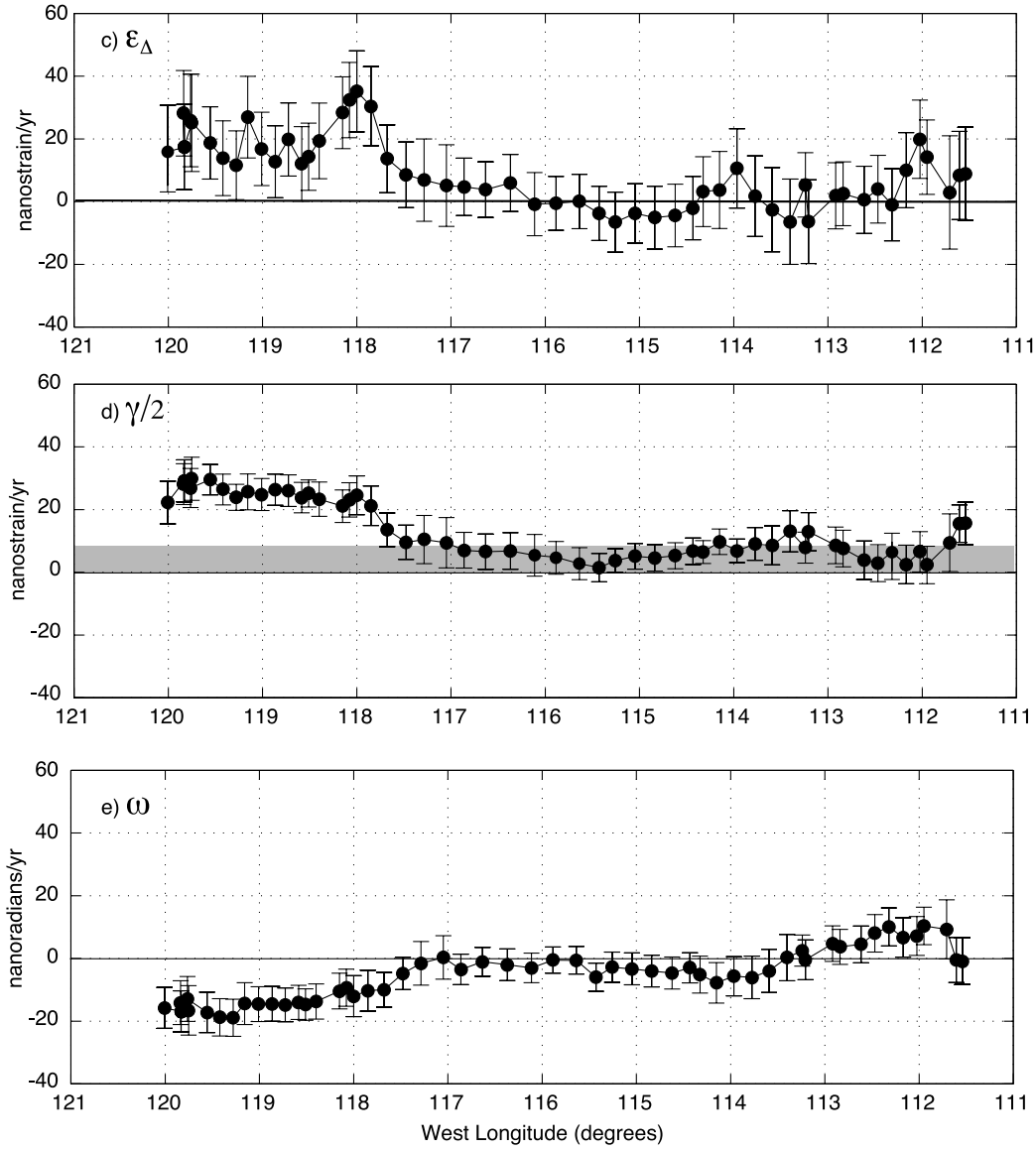

Figure 4. (continued)

and shear rate parallel to a vertical plane striking along the average direction of the CNSZ (N10°E) by rotating the coordinate axes by an angle $\theta = 10°$. The strain rates in the new (primed) coordinates are [*Turcotte and Schubert*, 1982]

$$\begin{aligned}\varepsilon'_{11} &= \varepsilon_{11}\cos^2\theta + \varepsilon_{22}\sin^2\theta + \varepsilon_{12}\sin 2\theta,\\ \varepsilon'_{22} &= \varepsilon_{11}\sin^2\theta + \varepsilon_{22}\cos^2\theta - \varepsilon_{12}\sin 2\theta,\\ \varepsilon'_{12} &= 0.5(\varepsilon_{22} - \varepsilon_{11})\sin 2\theta + \varepsilon_{12}\cos 2\theta.\end{aligned} \tag{3}$$

In Group 3 the normal extension across the fault is ε'_{11} = 32.6 ± 10.9 nstr/yr, and the shear strain rate is ε'_{12} = 22.9 ± 6.3 nstr/yr in the right lateral sense. This vertical plane is not intended to represent any particular fault in the CNSZ but represents the zone as a whole, so we use a 90° dip. If this model is an appropriate interpretation of the deformation field, then ε'_{22} should be zero [*Svarc et al.*, 2002]. After rotation, ε'_{22} = 2.4 ± 8.0 in Group 3, indicating that the deformation can be described as normal and dextral slip on a plane striking N10°E.

[20] Farther west, between 118.4°W and 119.3°W within the northern Walker Lane Belt, the deformation is right lateral simple shear. There is no significant dilatation (ε_Δ = 3.3 ± 9.0 nstr/yr), unlike the areas to the west and east. For the seven sites within Group 2 the maximum shear rate is 20.6 ± 4.8 nstr/yr. The rotation rate implies dextral simple shear with direction of maximum extension oriented N56.0°W ± 3.0°. The deformation is consistent with shear across a vertical plane striking N13°W, different than the orientation of the WL and the Pacific–North America relative motion. If we rotate the coordinate axes to coincide with the average trend of the WL (∼N35°W), we find normal extension 13.6 ± 6.8 nstr/yr and right lateral shear 13.8 ± 4.5 nstr/yr parallel to the WL. Parallel to the fault is 16.9 ± 6.1 nstr/yr of contraction, suggesting that Group 2 deformation cannot be simply described as extension nor-

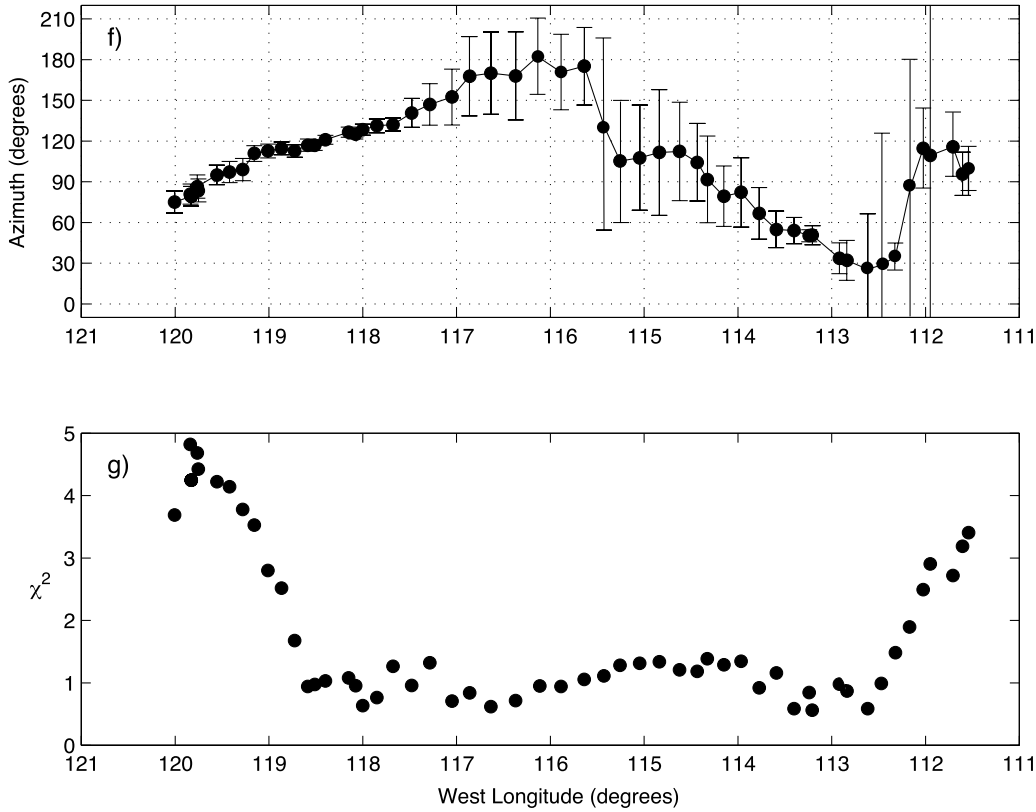

Figure 4. (continued)

mal to and shear parallel to a zone oriented N35°W. The presence of northeast striking left lateral and north striking normal faults [*Briggs et al.*, 2000] suggests that inside the WL the deformation is more complex than motion across faults oriented N35°W.

[21] At the westernmost end of our network, between 119.3°W and 120.5°W, in the vicinity of the Lake Tahoe and the Sierra Nevada frontal fault zone, the deformation is a combination of dextral shear and extension ($\varepsilon_1 = 41.5 \pm 6.1$, $\varepsilon_2 = -15.0 \pm 5.8$, and $\omega = -19.3 \pm 4.1$ nstr/yr, Group 1 of Table 3). The azimuth of maximum extension (N76.7 ± 4.2°W) is rotated counterclockwise compared to the WL region to the east. This change is correlated with a change in the strike of the normal faults (Figure 1) and is addressed more thoroughly below. Extension normal to a north striking fault is 38.5 ± 6.1 nstr/yr, and the fault parallel shear is 12.6 ± 4.1 nstr/yr right lateral. Contraction in the direction parallel to the fault is −12.0 ± 5.8 nstr/yr, suggesting that the deformation is not quite completely explained as normal extension plus right lateral shear across a north striking fault. An alternative interpretation of Group 1 deformation is extension accommodated on north striking normal faults combined with shear accommodated on N35°W trending dextral slip faults. We can assess whether this model is capable of explaining the deformation by applying equation (3) with $\theta = -35°$ to determine the portion of shear attributable to this fault and then finding the deformation remaining after this shear is removed. The result is that 19.4 ± 4.2 nstr/yr shear deformation is accommodated across N35°W planes, with 22.0 ± 6.1 nstr/yr normal extension and 23.5 ± 4.1 nstr/yr strike-slip remaining attributable to the north striking fault. No contraction parallel to the north striking fault remains, suggesting that this description is adequate. It is, however, not uniquely determined. The χ^2 misfit for any constant strain rate model is high inside Group 1 (Figure 4g), indicating that the strain rate field is more spatially variable than in the central Basin and Range. There is more complexity in the deformation of the transition between the WL and the SNGV.

[22] The negative slope of $v_\perp$ (Figure 2d) between Fairview Peak–Dixie Valley and the Egan Range suggests a small contraction. Grouping the sites between 117.9°W and 114.7°W and estimating a single constant strain rate tensor results in a statistically significant contraction of $\varepsilon_2 = -4.7 \pm 1.5$ nstr/yr ($\chi^2 = 1.0$) with azimuth of N73.6 ± 13.5°W, while ε_1 is not significant. The total velocity variation required to obtain this low rate contraction is ∼1.4 mm/yr across ∼280 km and is distributed roughly evenly over this distance. This contraction is still significant in smaller subsets of the above sites as long as the baseline is greater than 200 km. Thus this contraction is not an artifact of one or two anomalous velocities. Groups of sites over apertures narrower than 200 km display no statistically significant deformation.

[23] The domains described are distinct regions with different deformation styles. To test the significance of these differences, we use the misfit statistic χ^2 to describe the appropriateness of a constant strain rate model (Figure 4g). When $\chi^2 \gg 1$, the velocities are poorly fit by a constant strain rate model and the deformation within that group is more spatially variable. Comparing the result of combining the Groups 1, 2, and 3 together ($\chi^2 = 4.9$ in Table 3) to their

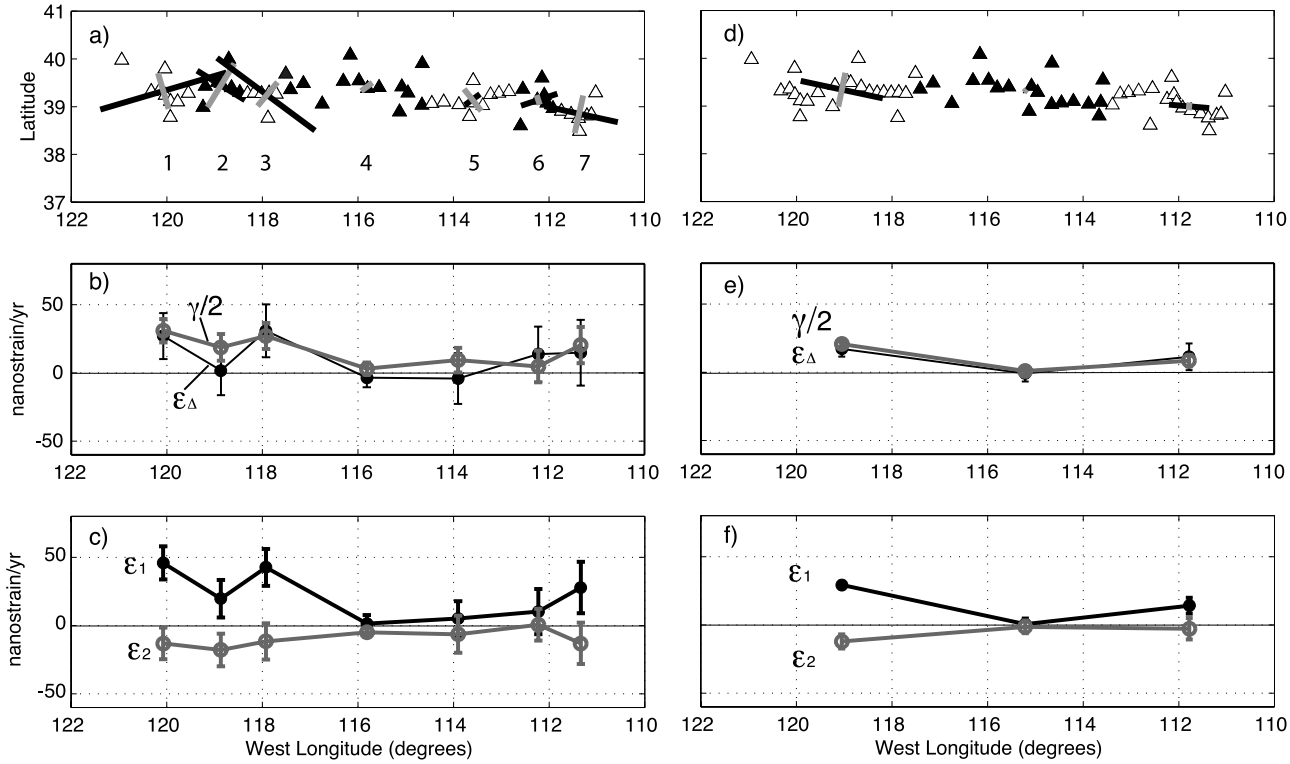

Figure 5. Figures 5a and 5d show tensor strain rates for two subdivisions of GPS sites. Black bar indicates direction and magnitude of maximum extensional rate, and gray bar shows direction and amplitude of maximum contraction rate. Triangles are alternately shaded black and white to indicate GPS site subsets, with group number, referenced in Table 3, below. Figures 5b and 5e show magnitude and uncertainty (2σ) in the dilatation rate ε_Δ (black) and maximum shear strain rate $\gamma/2$ (gray). Figures 5c and 5f are the maximum principal strain rate ε_1 (black) and minimum principal strain rate ε_2 (gray) and uncertainty (2σ). Strain rate values are also given in Table 3.

individual results shows that the data are better fit when strain rates are estimated individually to a confidence level of 85% determined by an *F* test. The width of the moving window restricts high misfit to the western 100 km of the network, near Group 1, where maximum $\chi^2 \approx 5.0$, and to the eastern 80 km of the network, where maximum $\chi^2 \approx 4.8$. Thus there is more variability in the strain rate field where the deformation is fastest. The strain rates exhibited in the rest of the Basin and Range such as the simple shear inside the WL, extension and shear in the CNSZ, and low rate extension near the NV/UT border are well estimated by a constant strain rate field. The regions of highest variability in strain rate are at the extreme boundaries of the Basin and Range province, where the velocity gradients are highest.

4.2. Utah

[24] At the east end of the network, near longitude 111.5°W and the WFZ, we find extension (ε_1 = 24.4 ± 9.4 nstr/yr) oriented N76.6° ± 9.9°W (Group 7 of Table 3). Rotation and ε_2 are not significant, indicating that this deformation is best characterized as uniaxial extension. This strain rate is, to within 95% confidence, consistent with that observed by *Bennett et al.* [1998, 2003], who found 21 ± 2 nstr/yr, and *Martinez et al.* [1998], who found 49 ± 23 nstr/yr across the WFZ farther north, in the vicinity of Great Salt Lake. Misfit to a constant strain rate model is among the highest observed (χ^2 = 5.7, Table 3), indicating that the deformation is spatially inhomogeneous. Inspection of Figure 2d suggests that the region over which extension is significant possibly extends from the NV/UT border to the east end of the network. However, ε_1 in Groups 5, 6, and 7 are 5.2 ± 4.8, 13.3 ± 8.3, and 24.4 ± 9.4, respectively, suggesting an extension rate that increases to the east.

5. Discussion

5.1. Basin and Range Kinematics

5.1.1. Comparisons With a Nearby Continuous GPS Network

[25] To first order the reported results from the Basin and Range Geodetic Network (BARGEN) (Figure 1) of *Wernicke et al.* [2000] and *Bennett et al.* [2003] are consistent with ours. We find similar total velocity change across the Basin and Range, similarly higher strain rates within the CNSZ and west of it, and a strong component of right lateral shear and extension inside the WL. The largest disagreement occurs in the central Great Basin between 114°W and 117°W. *Wernicke et al.* [2000] found a nearly linear increase in the east velocity with longitude (with the exception of the site LEWI near longitude 117°W) through the entire Great Basin, indicating uniform east-west exten-

Table 3. Strain Rate Components with 1-σ Uncertainties for Selected Subnetworks[a]

	Group 1	Group 2	Group 3	Group 4	Group 5	Group 6	Group 7
Long.	−120.1	−118.9	−118.0	−115.9	−113.9	−112.2	−111.3
ε_1	41.5 ± 6.1	22.2 ± 6.8	44.5 ± 9.7	1.2 ± 2.9	5.2 ± 4.8	13.3 ± 8.3	24.4 ± 9.4
ε_2	−15.0 ± 5.8	−18.9 ± 6.2	−11.5 ± 8.8	−4.6 ± 1.9	−11.3 ± 5.8	1.0 ± 5.9	−14.7 ± 7.7
$\gamma/2$	28.2 ± 4.3	20.6 ± 4.8	28.0 ± 6.8	2.9 ± 2.1	8.3 ± 3.4	6.2 ± 5.8	19.5 ± 6.6
$\varepsilon\Delta$	26.5 ± 8.4	3.3 ± 9.3	32.9 ± 13.5	−3.4 ± 3.4	−6.1 ± 7.6	14.2 ± 10.2	9.6 ± 12.1
α	76.7 ± 4.2°	−56.0 ± 3.0°	−52.6 ± 2.8°	−26.2 ± 10.5°	55.3 ± 10.6°	71.9 ± 20.5°	−76.6 ± 9.9°
ω	−19.3 ± 4.1	−17.8 ± 4.5	−24.8 ± 6.3	−2.7 ± 1.8	−4.1 ± 3.7	14.3 ± 5.0	−5.6 ± 6.2
χ^2	5.0	2.7	0.9	1.2	1.4	1.7	4.8

	Groups 1+2+3	Groups 4+5	Groups 6+7	−114 to −112	−112 to −110	−115 to −112.8	CNSZ
Long.	−119.1	−115.3	−111.8	−112.9	−111.3	−113.9	−118.1
ε_1	30.9 ± 1.3	1.5 ± 1.5	13.9 ± 2.9	5.6 ± 3.2	10.6 ± 6.9	7.9 ± 2.1	34.6 ± 3.8
ε_2	−14.0 ± 2.6	−3.4 ± 2.6	−3.5 ± 3.9	−6.5 ± 3.3	−15.7 ± 7.0	−6.5 ± 3.7	−6.2 ± 4.5
$\gamma/2$	22.5 ± 1.0	2.4 ± 1.1	8.7 ± 2.1	6.0 ± 2.3	13.2 ± 4.9	7.2 ± 1.5	20.4 ± 2.7
$\varepsilon\Delta$	17.0 ± 2.9	−1.9 ± 3.0	10.4 ± 4.9	−0.9 ± 4.4	5.1 ± 9.9	1.4 ± 4.3	28.3 ± 6.0
α	−79.6 ± 2.1°	−63.2 ± 20.3°	−86.3 ± 8.6°	45.4 ± 1.0°	−82.1 ± 16.2°	82.8 ± 11.1°	−54.8 ± 2.0°
ω	−19.5 ± 1.6	−2.4 ± 1.5	5.1 ± 2.4	4.8 ± 2.4	−6.0 ± 5.0	−0.9 ± 2.1	−8.7 ± 2.9
χ^2	4.9	1.6	3.2	1.0	4.4	1.7	1.9

[a]Symbols are as follows: α is geographic azimuth of axis of maximum extension, measured clockwise from north, ε_1 and ε_2 are first and second principal strain rates, respectively, $\gamma/2 = (\varepsilon_1 - \varepsilon_2)/2$ is maximum shear rate, $\varepsilon\Delta = \varepsilon_1 + \varepsilon_2$ is dilatation rate, ω is clockwise negative rotation rate around the vertical axis, and χ^2 is misfit of uniform strain rate model defined in equation (2). Group 1: A210, A220, A250, A270, A275, A280, A281, A300, P2 = 08, QUIN, SAGE, UU83. Group 2: A290, B100, B200, B210, B220, B230, B300, RATT. Group 3: BX46, B270, B280, B290, C200, C300. Group 4: C100, C220, C240, C260, C280, D100, D200, D220, D240, D260, D280, D300, E100, E200, E220, E300. Group 5: E240, E260, E280, F100, F200, F220, F230, F250, F270, F300. Group 6: F280, G100, G101, G200, G210, G220, G230, G300. Group 7: G250, G270, G280, G290, H100, H200, H300. Group CNSZ: Group 3 with B200, B210, B220, B230, C100, C220. Group −112 to −110: G230, G250, G270, G280, G290, H100, H200, H300. Group −114 to −112: E280, F100, F200, F220, F230, F250, F270, F280, F300, G100, G200, G210, G220, G300. Group −115 to −112.8: E100, E200, E220, E240, E260, E280, F100, F200, F220, F230, F250, F270, F300.

sion of ∼10 nstr/yr. *Bennett et al.* [2003] characterize the central Great Basin, with the addition of 1–2 more years of continuous GPS data and up to 6 years of our [*Thatcher et al.*, 1999] campaign GPS measurements, as a "geodetic microplate" with no resolvable east-west extension but a small component (5.1 ± 1.5 nstr/yr) of north directed right lateral shear. Our results show extension (7.9 ± 2.1 nstr/yr, Table 3) between 112.8°W and 115°W and contraction (4.7 ± 1.3 nstr/yr) between 114.7°W and 117.9°W. These estimates use intersecting but not congruent subsets of the GPS data in the central Great Basin, and hence our disagreement may be due to differences in network location or site selection.

[26] At the east end of the Basin and Range the largest strain rate is near 111.5°W, between the BARGEN sites SMEL and CAST. *Niemi et al.* [2004] infer that the nearby BARGEN sites EGAN, FOOT, SMEL, and CAST (Figure 3) show an east velocity that varies linearly as far west as 115°W, implying a strain rate of about 11 nstr/yr over a region ∼400 km wide. Taking our uncertainties into account, our velocities agree with those of *Niemi et al.* [2004] to within 95% confidence, but our denser station spacing indicates that the deformation is more concentrated. *Bennett et al.* [2003] make an interpretation similar to ours, with a strain rate that increases closer to the WFZ. When we group the 13 sites between 112.8°W and 115°W (Table 3), we find resolvable east-west extension centered just east of the NV/UT border, with $\varepsilon_1 = 7.9 \pm 2.2$ nstr/yr. This region is ∼180 km wide and has ∼1.8 mm/yr of velocity variation. This is less than half the rate seen at the WFZ (Figure 4a). The misfit of a uniform strain rate field to velocities between 112.8°W and 115°W is $\chi^2 = 1.7$, greater than misfit values in central Nevada. This is likely owing to a rotation of the azimuth of the extension axis between 113°W, where it is NE-SW, and 114°W, where it is approximately E-W (Figure 3).

[27] It is intriguing that the relatively low western velocity of the BARGEN continuous site LEWI, noted by *Wernicke et al.* [2000], occurs near 117°W longitude, close to the west end of the region where we have observed slight contraction in our GPS velocities. While LEWI lies roughly 100 km north of the main axis of our network, its longitude is close to that of site C100, which is at the west end of a region whose velocity we have found decreases with westward distance by ∼1.4 mm/yr over 280 km. However, the contraction we observe is much more gradual that that implied by the anomalously low velocity of LEWI.

5.1.2. Sierra Nevada–Great Valley Motion

[28] Our results are compatible with previous studies that have estimated the motion of the Sierra Nevada–Great Valley microplate (SNGV) with respect to stable North America [e.g., *Minster and Jordan*, 1987; *Argus and Gordon*, 1991, 2001; *Bennett et al.*, 1999; *Dixon et al.*, 2000; *Bennett et al.*, 2003]. The SNGV at the site QUIN moves approximately 11.3 ± 0.3 mm/yr in the direction N59°W. However, *Dixon et al.* [2000] have pointed out that the motion of QUIN is not representative of the rigid SNGV because it is affected by elastic strain accumulation on the Mohawk Valley fault, which bounds the SNGV to the east. They compute an Euler pole at 17.0°N latitude, 137.3°W longitude rotating at 0.28° per million years from sites in the interior of the block to avoid strain accumulation near the

edges of the SNGV. Our westernmost sites are similarly close to the eastern boundary of the SNGV. For the three sites closest to the SNGV interior (QUIN, UU83, A300), mean $v_{//}$ is 10.4 ± 0.9 mm/yr, and mean $v_{\perp}$ is 5.1 ± 0.9 mm/yr. The pole of *Dixon et al.* [2000] predicts mean motion of these sites to be 13.3 mm/yr and 4.3 mm/yr, respectively. Thus our westernmost sites appear to not quite attain the rigid motion of the SNGV interior. This is apparent from the deformation of our westernmost sites which is similar to that of the WL (Figure 2d).

5.2. Rate Debate: The Central Nevada Seismic Zone

5.2.1. Slip Rates

[29] In order to compare geodetically determined estimates of fault slip rate to geologically estimated slip rate, we must identify the set of GPS sites that capture all of the motion from the fault of interest while avoiding deformation attributable to other faults. A fault that slips at depth but is locked at the surface has a cross-fault horizontal velocity profile that approaches a constant far field value away from the fault, with the total offset rate equal to the horizontal component of fault slip rate. This characteristic behavior applies for both strike-slip [*Savage and Burford*, 1973] and dip-slip faults [*Freund and Barnett*, 1976]. Thus a slip rate determined from a network that does not span the entire zone of strain accumulation will yield an underestimate, while a slip rate derived from a very broad network could be contaminated by deformation associated with other faults. The CNSZ is bounded on the east by a nearly nondeforming region and on the west by the right laterally straining WL. Thus, in order to bound the deforming zone of the CNSZ to the west we consider two subnetworks. Motion of the sites in Group 3 (Table 3) includes the deformation associated with the Fairview Peak, West Gate, and Gold King faults and will likely provide a lower bound for the combined average slip rate on these faults. If we increase the number of sites to include B220, B230, C100, and RATT (see Figure 1b and Table 3, column marked CNSZ), then motion of these sites will also be sensitive to the Rainbow Mountain and Dixie Valley faults, which lie just north of Highway 50. In this larger subnetwork the extension axis is rotated counterclockwise, and a small amount of shear strain (significant ε_2 in Table 3) is present. Therefore including these sites adds some of the dextral shear strain of Group 2, as well as including deformation associated with the CNSZ.

[30] To estimate the slip rate, we project the velocity variation normal and parallel to the average strike of the CNSZ (N10°E). Velocity difference inside Group 3 is 1.5 ± 0.3 mm/yr right lateral and 1.7 ± 0.6 mm/yr extensional (total rate of 2.2 ± 0.6 mm/yr along N53°W). If we include the additional sites mentioned above, we obtain 2.3 ± 0.3 mm/yr right lateral and 3.0 ± 0.4 mm/yr extensional (total rate of 3.8 ± 0.5 mm/yr along N58°W). Thus the ratio of strike-slip to extensional motion is 0.7–1.0 for strain accumulation in the CNSZ subnetwork. This is different than the geodetic results of *Hodgkinson et al.* [1996], who studied the coseismic slip of the 1954 events using leveling and triangulation data and found a strike-slip to extension ratio of ~2–3. This discrepancy may be explained by strain accumulation or postseismic relaxation related to faults other than those that slipped in 1954.

[31] The paleoseismologically estimated slip rate on CNSZ faults is less than the rate inferred from GPS measurements. To make this comparison, the paleoseismic slip rate estimates must be resolved into their horizontal components from vertical or dip-slip offsets, which requires knowledge of the dip of the fault. Globally, the dips of seismically active normal faults are strongly clustered around 45° [*Thatcher and Hill*, 1991]. The CNSZ faults have dips estimated to be somewhat steeper than the global average, varying from 51° to 78° [*Doser*, 1986]. However, expected variations in fault dip are likely not great enough to account for the discrepancy. The cumulative paleoseismic slip rate magnitude across trenched faults in the CNSZ is between 0.5 and 1.3 mm/yr [*Bell et al.*, 2004]. Horizontal extension is derived from vertical slip using observed surface fault dips of 60° to 70°. Therefore the GPS velocity difference is 1.0 to 3.5 mm/yr greater than the paleoseismologically inferred rate. The disagreement between GPS and long-term estimates can also be illustrated using recurrence times of large earthquakes. If we use 2.4 mm/yr strike-slip motion and assume that the 1954 earthquakes are characteristic and occur periodically in time, then the horizontal strike-slip displacement of ~4.2 m (using Rainbow Mountain plus Fairview Peak in Table 8 of *Hodgkinson et al.* [1996]) implies a recurrence interval of ~1750 years. Using extensional motion of 3.2 mm/yr and 2.5 m of coseismic extension in 1954, we obtain a recurrence interval of ~780 years. This is far smaller than the recurrence intervals in central Nevada seen using geomorphic indicators, which are on the order of 10,000 years [*Wallace*, 1978]. They are also much smaller than the minimum time since the last events before 1954: e.g., >13,000 years for Rainbow Mountain and >35,000 years for Fairview Peak [*Caskey et al.*, 2000; *Bell et al.*, 2004]. Thus the relative motion determined from GPS measurements is too large to be consistent with paleoseismic estimates. There are at least three possible explanations: (1) present-day rates are much greater than those inferred for the past 10 to 40 kyr, (2) a significant proportion of motion is being accommodated across other faults near the CNSZ, or (3) there is a significant contribution from postseismic relaxation following the historic CNSZ events.

5.2.2. Effects of Postseismic Relaxation

[32] The inconsistency between the geodetically and geologically inferred slip rates may be explained by the presence of viscoelastic strain relaxation owing to the 1954 earthquakes. *Wernicke et al.* [2000] have discussed the possibility of transient waves of strain propagating away from the CNSZ earthquakes. However, they use a two-dimensional model with an elastic layer overlying a purely viscous lower crust that significantly overestimates the postseismic strain rates [*Hetland and Hager*, 2003] (hereinafter referred to as HH). Three-dimensional viscoelastic relaxation of the lower crust and upper mantle following the 1915 Pleasant Valley (M_W = 7.5), 1932 Cedar Mountain (M_S = 7.2), 1954 Fairview Peak (M_W = 7.1), and 1954 Dixie Valley (M_W = 6.8) earthquakes has been modeled by HH assuming a variety of viscosity values. Their preferred model is designed to best explain the contraction east of the CNSZ measured by *Thatcher et al.* [1999] and observed in the present study. Their model has a 15 km thick elastic upper crust, a 15 km thick Maxwell Newtonian viscoelastic lower crust ($\eta_{LC} = 10^{19}$), and a viscoelastic half-space upper

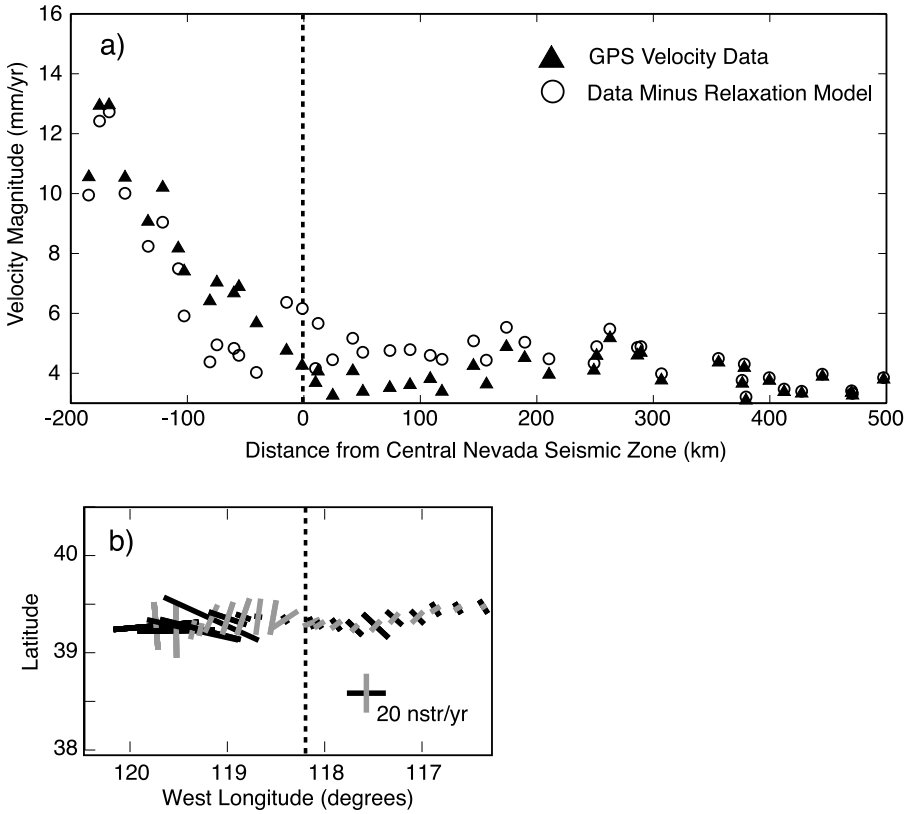

Figure 6. (a) GPS velocity magnitude (triangles) showing east-west contraction between 0 and 250 km east of the CNSZ and velocity after removal of viscoelastic relaxation of the lower crust and upper mantle following the historic earthquakes in the CNSZ as modeled by *Hetland and Hager* [2003] (circles). Their model uses a viscosity of the lower crust ($\eta = 10^{19}$ Pa s) that is one tenth that of the upper mantle. (b) Close-up view of horizontal strain rate tensor as in Figure 3, but with the modeled relaxation subtracted from the GPS velocities. Almost all deformation near the CNSZ (dotted vertical line) has been removed. Note that Figures 6a and 6b have different horizontal axes.

mantle ($\eta_M = 10\eta_{LC}$). Their resulting relaxation velocities vary by approximately 4 mm/yr peak to peak in the time and location that our data were collected and are near zero at great distances from the CNSZ. We estimate the time-invariant secular motion by subtracting the relaxation velocities from our GPS velocities (Figure 6). The result shows that the long-wavelength contraction observed in this study is removed. However, nearly all the deformation near the CNSZ is also removed, which may be an overcorrection since some interseismic strain accumulation is needed to drive the CNSZ faults to rupture. Furthermore, our velocities minus the HH model show a sharp negative offset of ~2.5 mm/yr near the 1954 ruptures (Figure 6a). This offset is not present in the observed velocities and is unlikely to be a feature of the steady state deformation field. This offset is the cause of the unlikely north-south secular contraction west of the CNSZ (Figure 6b) and may be the result of using a coseismic model with less strike-slip displacement than is appropriate [*Hodgkinson et al.*, 1996]. Thus the HH model suggests that the deformation field includes a significant component of postseismic relaxation at the CNSZ, but the specific model proposed by HH may distort the true steady state velocity field. Transients like those in the HH model are large enough to be important in understanding the discrepancy between geodetic and geologic slip rates and imply viscosity structures similar to those found in other studies of the western United States [e.g., *Nishimura and Thatcher*, 2003]. However, more study will be required to conclusively separate the time-invariant and postseismic components of deformation.

5.2.3. Regional Relationship Between Faulting and Contemporary Deformation

[33] Present-day deformation measured with GPS is similar to deformation that has occurred through the Quaternary. If the long-wavelength GPS velocity field is representative of extensional deformation that occurs over timescales greater than the earthquake cycle, then the azimuth of extension should be subperpendicular to the range-bounding normal faults. However, the presence of strike-slip motion reduces the angle between the extension azimuth and fault strike. Figure 7 shows the distribution of fault azimuths as a function of longitude for three longitude bins that span the CNSZ, WL, and SNGV. This figure was made from the U.S. Quaternary Faults and Folds Database, in production by the Central Earthquake Hazards Team of the U.S. Geological Survey (R. Dart, personal communication, 2002), with individual fault segments stitched together into larger contiguous faults and the final azimuth taken from the line joining the first and last points of the joined line segment. The correlation between the strike of faults active over the

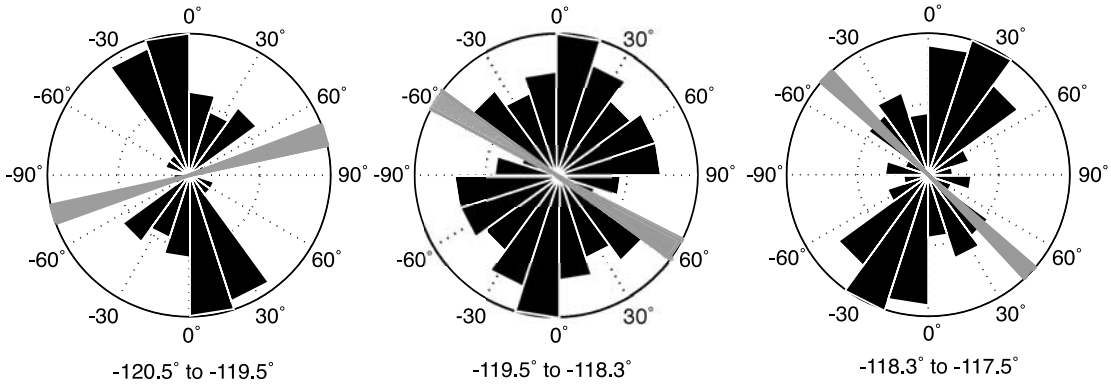

Figure 7. Rose plots show distribution of Quaternary fault segment azimuths (black wedges) between 38° and 40° latitude inside the three longitude bins indicated. Gray wedges bound ±1 standard deviation around the azimuth of maximum GPS extension rate for the sites whose centroid has the mean longitude of the bin.

Quaternary and the contemporary geodetic deformation suggests that GPS motion represents long-term deformation. The change in average strike of the faults track, from east to west, the change in azimuth of the axis of maximum extension (Figures 7a–7c). Furthermore, the faults near the CNSZ make an average angle approximately 75°–80° from the axis of geodetic extension (Figure 7c), consistent with our conclusion that the CNSZ accommodates extension and right lateral shear. Figure 7 indicates that this also holds true for the larger collection of faults active over the Quaternary.

5.3. Continental Dynamics: Basin and Range Scale Deformation

5.3.1. Rheological Weakness at the Walker Lane Belt

[34] Why is the deformation concentrated in the westernmost 200 km of the Basin and Range province? The orientation of shear deformation strongly suggests that the shear stresses have the same origin as those found in the San Andreas fault system. Stresses originating from the PA/NA relative plate motion are likely transmitted through the SNGV, deforming the western Basin and Range. However, inspection of Figures 4c and 4d shows that both the extension and shear deformation are concentrated near the WL, suggesting that it is a zone of rheological weakness. Is the observed concentration of deformation a result of rheological weakness of the WL, or is it attributable to the pattern of stress that is applied to boundaries of the Basin and Range lithosphere? To address this question, we consider briefly the forces that drive Basin and Range deformation and how they may generate the motions that we observe.

[35] The long-wavelength pattern of deformation is likely caused by some combination of shear tractions across the Pacific–North American plate boundary and extension driven by lateral density gradients in the crust and mantle of the western U.S. interior. Lateral density variations lead to differences in gravitational potential energy (GPE) that can drive deformation [e.g., *Frank*, 1972; *England and McKenzie*, 1982; *Coblentz et al.*, 1994]. Three mechanisms can drive extension in the interior western United States: (1) excess GPE in the Basin and Range lithosphere [e.g., *Jones et al.*, 1996], (2) a divergent component to Pacific–North America plate motion manifested as distributed extension near the plate or microplate boundary, or (3) tractions exerted at the base of the lithosphere owing to mantle convection. These three cases differ according to the role of GPE variations within the Basin and Range in driving extension. In case 2 we explicitly consider the possibility that western retreat of the SNGV (perhaps owing to its own GPE difference with respect to the Pacific basin) is the primary cause of Basin and Range extension.

[36] For a thin viscous sheet overlying an inviscid fluid, force balance and depth (z component) invariance of stress and strain require that [e.g., *England and Molnar*, 1997; *Flesch et al.*, 2001]

$$\begin{aligned}\frac{\partial \tau_{xx}}{\partial x}-\frac{\partial \tau_{zz}}{\partial x}+\frac{\partial \tau_{xy}}{\partial y}&=\frac{\partial \Gamma}{\partial x},\\ \frac{\partial \tau_{yy}}{\partial y}-\frac{\partial \tau_{zz}}{\partial y}+\frac{\partial \tau_{xy}}{\partial x}&=\frac{\partial \Gamma}{\partial y},\end{aligned} \tag{4}$$

where x and y are horizontal Cartesian coordinates, Γ is the GPE per unit area, or, equivalently, the negative of the vertically averaged vertical stress, and τ is the deviatoric part of the stress tensor (extension reckoned positive). To provide a simple illustration, we assume a Newtonian incompressible fluid with viscosity η, expressed as

$$\tau_{ij}=\eta\varepsilon_{ij}, \tag{5}$$

where ε_{ij} is the ijth component of the strain rate tensor. We substitute equation (5) into equation (4) and assume that viscosity and GPE vary linearly in the x direction and do not vary in the y direction, obtaining

$$\eta\frac{\partial}{\partial x}(\varepsilon_{xx}-\varepsilon_{zz})+\frac{\partial \eta}{\partial x}(\varepsilon_{xx}-\varepsilon_{zz})=\frac{\partial \Gamma}{\partial x}, \tag{6}$$

$$\eta\frac{\partial \varepsilon_{xy}}{\partial x}+\frac{\partial \eta}{\partial x}\varepsilon_{xy}=0. \tag{7}$$

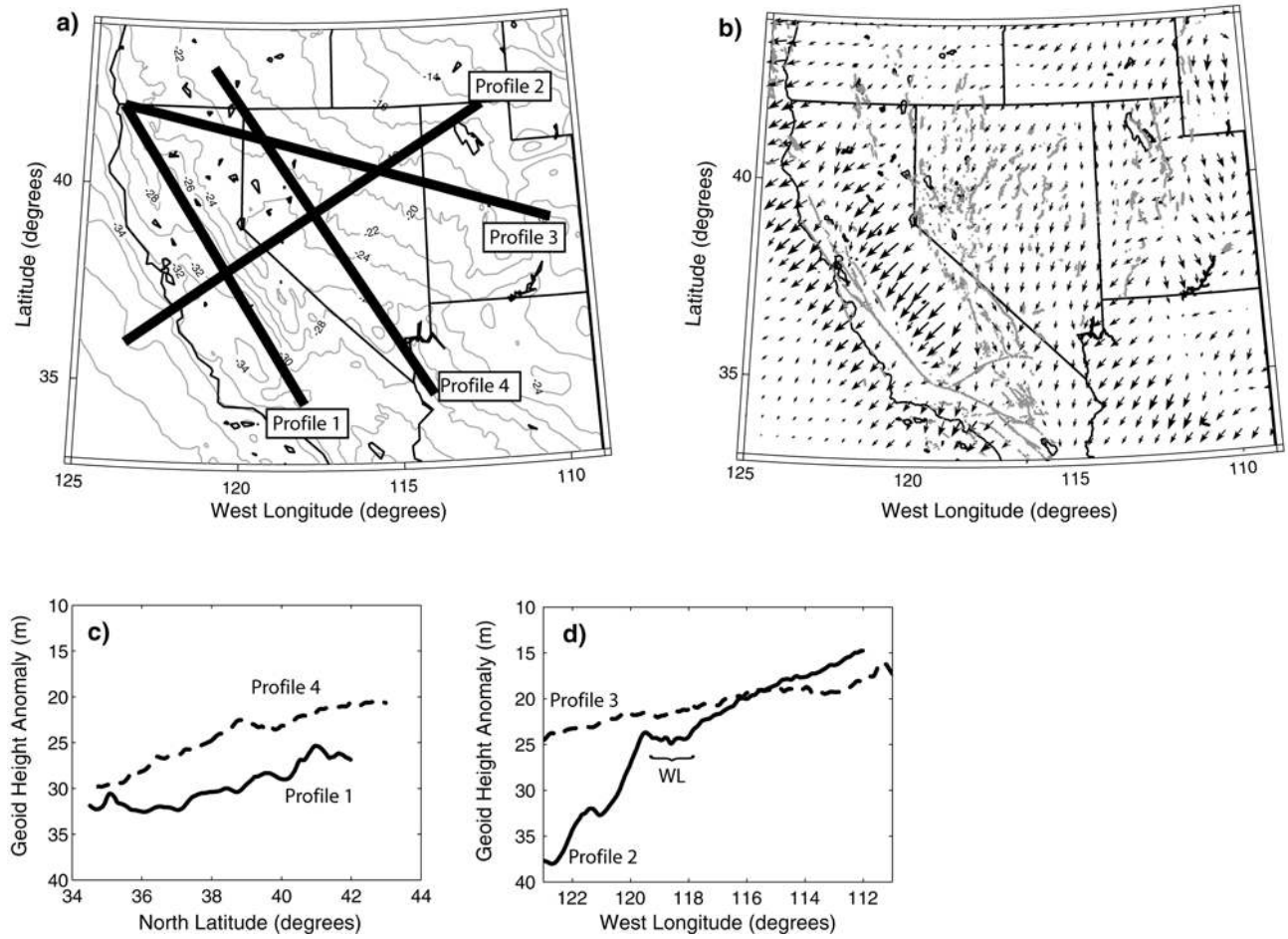

Figure 8. (a) Contours of the geoid anomaly (gray) in the Basin and Range, over U.S. state boundaries (black). Black bars give locations of the geoid profiles. (b) Historic and Holocene faults are gray, and direction and magnitude of horizontal gradient of the geoid, a proxy for horizontal force exerted by gravity, are black arrows. The geoid as a function of distance along the selected profiles is shown in Figures 8c and 8d. The geoid has a local minimum and an almost zero gradient where the greatest amount of GPS deformation and faulting have occurred in the Walker Lane Belt (WL).

The solutions to equations (6) and (7) are

$$\varepsilon_{xx} - \varepsilon_{zz} = \frac{\Gamma_0 + Ax}{\eta_0 + Bx}, \tag{8}$$

$$\varepsilon_{xy} = \frac{\eta_0 \varepsilon_{xy,0}}{\eta_0 + Bx}, \tag{9}$$

where $B = \partial\eta/\partial x$, $A = \partial\Gamma/\partial$x (both constants since we assume $\eta = \eta_0 + Bx$, $\Gamma = \Gamma_0 + Ax$), and $\varepsilon_{xy,0}$ is the xy strain rate at $x = 0$. Thus, if the viscosity and GPE vary linearly with x, the shear strain rates will vary with $1/x$, and deformation will become focused near the minimum viscosity. Since viscosity commonly varies by orders of magnitude, this focusing can be quite strong. Non-Newtonian rheologies will tend to concentrate gradients even more [*England and McKenzie*, 1982; *Thatcher*, 2003]. This model is generally consistent with the presence of high rates of active faulting in the western Basin and Range and very low rates in the east, where deformation rates are almost too low to be observed by our GPS measurements. Furthermore, equations (8) and (9) show that concentration of shear and extensional deformation can occur and coincide even when GPE gradients within the Basin and Range are relatively smooth and gradual. Indeed, extension can be concentrated even if GPE gradients are locally zero, consistent with case 2 above.

5.3.2. Western U.S. GPE Gradients

[37] Gradients in the unfiltered geoid (Figure 8) can be easily related to gradients in lithospheric GPE if we assume that the lithosphere is in isostatic balance and that all density variations causing the geoid deflection are in the lithosphere [*Coblentz et al.*, 1994]. Density variations in the sublithospheric mantle, however, may impose vertical tractions to the base of the lithosphere, causing a vertical deflection, i.e., dynamic topography. The length scale and depth of the density anomalies and viscosity structure control the pattern of uplift and extension [*Ricard et al.*, 1984]. Seismic tomography studies of the western United States suggest that such anomalies do exist [e.g., *Grand*, 1994; *Humphreys and Dueker*, 1994; *Hearn*, 1996; *van der Lee and Nolet*,

1997; *Dueker*, 1998]. Therefore sublithospheric density gradients may be contributing to the western U.S. geoid anomalies, and the relations among strain rate, geoid gradient, and GPE gradient are more complex than those in equations (4) through (9). However, any sublithospheric effects will be long wavelength ones and much of the analysis that follows is unaffected.

[38] As shown in Figure 8, the motions expected from the western U.S. geoid variation are at odds with the observed contemporary deformation. Because differences in geoid height are a proxy for GPE differences, the horizontal vector gradient in geoid anomaly points in the direction of motion expected for gravitational collapse. Four profiles of the GEOID99 model [*Smith and Roman*, 2001] (Figure 8a) show over 30 m of geoid variation across the western U.S. margin. Profiles 1 and 4 are tangent to the local small circle around the PA/NA pole of rotation. Profile 2 is normal to profiles 1 and 4, and profile 3 runs normal to the average strike of the range-bounding faults. Profile 2 shows two important features (Figure 8d). First, the direction normal to the plate boundary has the largest geoid gradient, steepest across the SNGV microplate. Second, a pronounced local minimum occurs exactly in the WL, where measured deformation is greatest. In fact, a general feature of the geoid in the western Basin and Range and near the San Andreas fault system is that geoid gradients are anticorrelated with geodetically measured velocity gradients. More specifically, the dilatational component of GPS strain rate is greatest west of 117.5°W (Figure 4a), where local GPE gradients are minimal. Thus other factors such as rheological variations and plate boundary tractions must guide deformation in the western Basin and Range. Note also that the GPE gradient along the length of the SNGV is small compared to the gradient normal to the PA/NA plate boundary, decreasing to the SE, in the direction opposite SNGV motion (Figure 8c, Profile 1). Thus the SNGV is most likely transported parallel to the plate boundary through tractions applied by the Pacific plate but moves normal to the plate boundary because of its strong plate boundary normal GPE gradient (Figure 8b and Profile 2).

[39] *Flesch et al.* [2000] have computed a horizontal tensor stress field owing to GPE variations and plate boundary tractions in the western United States that is largely consistent with our strain rates. However, their principal stress orientations were constrained to be coaxial with tensor strain rates they derived from earlier geodetic results for this region [e.g., *Thatcher et al.*, 1999; *Bennett et al.*, 1999]. Even so, *Flesch et al.* [2000] predict almost exclusively uniaxial extensional stress throughout most of the Basin and Range, whereas our results show a strong component of dextral shear that is concentrated in the westernmost 200 km of the province. This difference may be due to the noticeable GPE "ridge" shown in central Nevada [see *Flesch et al.*, 2000, Figure 2a]. This feature, not visible in the unfiltered GEOID99 model (Figure 8a), leads to roughly north-south oriented extensional stresses in this region. Extensional stresses from longer-wavelength GPE gradients will likely be oriented more normal to the plate boundary and may partially cancel the compressive component of the shear stress due to PA/NA tractions.

[40] The local minima in geoid height in the WL may have resulted from the concentrated lithospheric extension, thinning, and attendant reduction in surface topography over a time greater than the earthquake cycle. This view is consistent with paleoseismological evidence that faults east of the CNSZ have lower rates than those to the west [*Caskey et al.*, 2000]. *Wallace* [1984] suggested that Basin and Range deformation may have migrated east and west across the province during the Quaternary and only now resides at its current location. However, if the concentrated deformation in the WL is related to the anomalously high heat flow [*Lachenbruch and Sass*, 1978; *Morgan and Gosnold*, 1989], low upper mantle seismic *P* wave velocity [*Humphreys and Dueker*, 1994; *Dueker*, 1998], and high rate of recent magmatism over the late Cenozoic [*Armstrong and Ward*, 1991], then the deformation has likely been focused near the WL for times much longer than the Holocene, as suggested by *Dixon et al.* [2000]. These properties of the WL are all consistent with a zone of locally weaker lithosphere.

6. Conclusions

[41] We have estimated the rates of crustal movement across the Basin and Range province of the western United States using repeated measurements with the Global Positioning System (GPS). The rate of motion across the province in the direction normal to the small circle around the Pacific–North America pole of rotation is 5.1 ± 1.0 mm/yr with respect to nondeforming North America. If, as is commonly believed, the Basin and Range has stretched by a factor of 2 in the Cenozoic [e.g., *Hamilton*, 1978], then the current rate is smaller than the average rate over the last 35–45 Myr. The component of motion tangent to the small circle around the Pacific–North America pole of rotation is 10.4 ± 1.0 mm/yr with respect to nondeforming North America. Compared to the east end of the network, the three westernmost sites, QUIN, UU83, and A300 (Figure 1a), move 10.4 ± 0.6 mm/yr parallel and 3.9 ± 0.6 mm/yr normal to the PA/NA relative motion. However, these sites may move more slowly than the rigid SNGV because of strain accumulation on the eastern margin of the SNGV.

[42] A transition in GPS velocity in the Basin and Range occurs near longitude 117.7°W, in the vicinity of the ruptures of the historic Dixie Valley, Fairview Peak, and Rainbow Mountain earthquakes. This transition is marked by (1) a change from a slowly deforming or nondeforming central and eastern Nevada and Utah to a region undergoing a higher rate of shear and extensional deformation to the west and (2) a significant change in the azimuths of velocity and extension.

[43] The observed deformation is concentrated across the Wasatch Fault Zone (WFZ) and in the westernmost 200 km of the network, in the vicinity of the Central Nevada Seismic Zone (CNSZ), Walker Lane Belt (WL), and Sierra Nevada frontal fault zone. Strain rate analysis of the GPS velocities shows that the style of deformation varies across subregions of the Great Basin. These regions are characterized by extension in the CNSZ, right lateral simple shear inside most of the WL, and extension superimposed on right lateral shear near the Sierra Nevada. The WFZ experiences approximately east-west uniaxial extension. Additionally, a much lower rate of extension between 112.8°W and 115°W (ε_1 = 7.9 ± 2.1 nstr/yr) and of approximately east-west

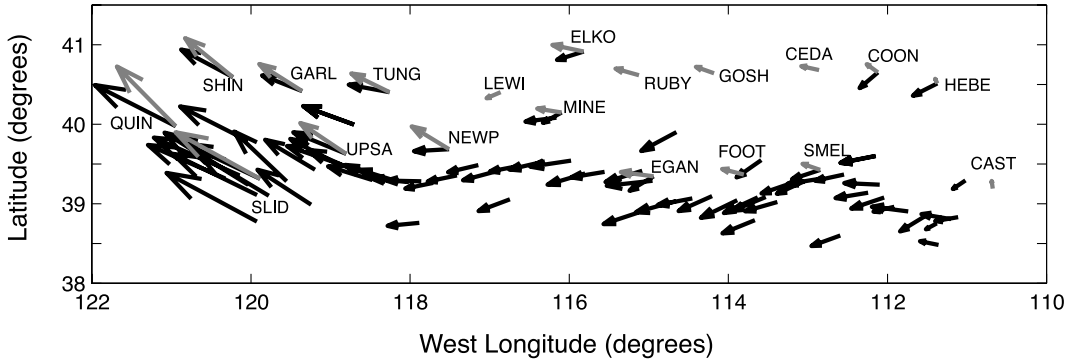

Figure A1. GPS velocities obtained from our analysis of campaign GPS data and from the subset of the BARGEN stations (COON, EGAN, ELKO, GARL, HEBE, MINE, QUIN, SHIN, SLID, TUNG, UPSA, and SMEL) for which we calculated velocities (black) and velocities for the BARGEN sites published by *Wernicke et al.* [2000] (gray).

contraction ($\varepsilon_2 = -4.7 \pm 1.5$ nstr/yr) between 117.9°W and 114.7°W longitude may be present.

[44] Deformation patterns are not spatially correlated with gradients in gravitational potential energy (GPE), as might be expected if the lithosphere were characterized as a homogenous fluid layer that is collapsing under its own weight. Instead, we find that deformation and GPE gradients throughout the WL and San Andreas fault system are spatially anticorrelated. Dilatational strain rates are greatest where gradients in GPE are minimal. This behavior is consistent with the WL being a zone of rheological weakness, deforming owing to Pacific–North America plate boundary shear tractions and lesser amounts of extension associated with long-wavelength GPE gradients.

[45] The concentration of deformation in the Walker Lane Belt is correlated with anomalous topography, high heat flow, late Cenozoic magmatism, an east-west transition in the average strike of major faults, and low *P* wave velocities in the upper mantle. This suggests that present-day deformation is representative of that occurring in the Holocene and late Quaternary.

Appendix A: Reference Frame

[46] We have chosen to present velocities in a North America reference frame, and hence the quoted uncertainties include that of the site velocity with respect to the neighboring stations and uncertainty in the velocity of the entire network with respect to nondeforming North America. In general, GPS measurement of position within an external reference frame (e.g., ITRF97, ITRF2000, North America) is less precise than estimation of relative station positions within a local network. To better understand the uncertainty in our reference frame realization, we have compared our velocities to those of *Wernicke et al.* [2000] (Figure A1). To make this comparison, we processed data from the BARGEN continuous sites, COON, EGAN, ELKO, GARL, HEBE, MINE, QUIN, SHIN, SLID, TUNG, UPSA, and SMEL, for each day that we also had available campaign data, estimating velocities using the same method we used on our own data. We then solve for the best three rotation rates, three translation rates, and one scale rate explaining the differences between our velocities and theirs. The resulting transformation explains a mean systematic difference of approximately 1.6 mm/yr, mostly in the north component. This systematic offset explains 78% of the RMS difference between the two velocity sets and indicates that most of the discrepancy can be attributed to differences in reference frame.

[47] We define the reference frame as ITRF2000 rotated so that the velocities of stations on the approximately nondeforming part of North America have as close as possible to zero velocity (pole latitude $-5.036° \pm 1.142°$, longitude $-83.144° \pm 1.945°$, rotating at $0.194° \pm 0.003°$ per million years [*Altamimi et al.*, 2002]). For each GPS day, data from the global tracking network of 51 IGS stations are processed using precise point positioning, as in the processing of the local stations. These 51 stations are a part of the definition of ITRF2000, and hence they strongly constrain our Helmert transformation into the North America frame. Positions on the given GPS day are extrapolated from 1 January 1997, and internal constraints are applied to the resulting reference frame to remove ambiguity in the location of the network. Finally, the daily GPS solution is transformed into the North America reference frame using a seven-parameter Helmert transformation.

[48] The choice of stations defining nondeforming North America has an impact on the reference frame. Vertical site motions from postglacial rebound in the otherwise stable cratonic interior are expected to be as large as ~10 mm/yr [*Larson and van Dam*, 2000] and affect the horizontal component of GPS velocity by a lesser amount. Previous studies focusing on the rigidity of the North American plate have found that residual velocities for these sites, after subtracting a rigid plate motion, are within 2 mm/yr [*Bennett et al.*, 1999], roughly the magnitude of the difference between our results and those of the BARGEN continuous network. To obtain an estimate for the variability of the velocity of the reference frame as a function of GPS sampling of North America, we have estimated the uncertainty in velocity in central Nevada due to uncertainty in the North America reference frame by iteratively deselecting one station from the above mentioned set of 13 sites and computing the effect this change has on station velocity. The resulting variation in velocity in central Nevada is approximately 0.2 mm/yr. This likely represents a lower

bound on the uncertainty in our North America reference frame since it does not include uncertainty associated with any bias in sampling North America or any unknown local motions at sites that have been assumed stationary.

[49] **Acknowledgments.** We thank Jim Savage, Will Prescott, and Jerry Svarc for numerous fruitful discussions. GPS data collection in September 2002 was made possible by the hard work of Beth Bartel, Steve Borenstein, Wade Cooksey, Jeanette Hagan, Auna Moser, Takuya Nishimura, Marleen Nyst, Shad O'Neel, Chuck Stiffler, Jim Sutton, Henry van den Bedem, Brian Wernicke, Chuck Wicks, and Tim Wright. Thanks go to Eric Hetland for providing his modeling results shown in Figure 6 and to Thomas Dewez for Figure 1. M. Machette and R. Dart provided the Quaternary Fault and Fold database of the western United States. This manuscript was greatly improved through thoughtful reviews of Jim Savage, Mary Lou Zoback, Yehuda Bock, Rob McCaffrey, and Don Argus.

References

Agnew, D. C. (1992), The time-domain behavior of power law noises, *Geophys. Res. Lett.*, *19*(4), 333–336.

Altamimi, Z., P. Sillard, and C. Boucher (2002), ITRF2000: A new release of the International Terrestrial Reference Frame for earth science applications, *J. Geophys. Res.*, *107*(B10), 2214, doi:10.1029/2001JB000561.

Argus, D. F., and R. G. Gordon (1991), Current Sierra Nevada-North America motion from very long baseline interferometry: Implications for the kinematics of the western United States, *Geology*, *19*(11), 1085–1088.

Argus, D. F., and R. G. Gordon (2001), Present tectonic motion across the Coast Ranges and San Andreas fault system in Central California, *Geol. Soc. Am. Bull.*, *113*(12), 1580–1592.

Armstrong, R. L., and P. Ward (1991), Evolving geographic patterns of Cenozoic magmatism in the North American Cordillera: The temporal and spatial association of magmatism and metamorphic core complexes, *J. Geophys. Res.*, *96*(B8), 13,201–13,224.

Bell, J. W., S. J. Caskey, A. R. Ramelli, and L. Guerrieri (2004), Pattern and rates of faulting in the 1932–1954 portion of the Central Nevada Seismic Belt, paleoseismic evidence for prior belt-like behavior, and comparison of fault and contemporary (GPS) slip rates., *Bull. Seismol. Soc. Am.*, in press.

Bennett, R. A., B. P. Wernicke, and J. L. Davis (1998), Continuous GPS measurements of contemporary deformation across the northern Basin and Range province, *Geophys. Res. Lett.*, *25*(4), 563–566.

Bennett, R. A., J. L. Davis, and B. P. Wernicke (1999), Present-day pattern of Cordilleran deformation in the western United States, *Geology*, *27*(4), 371–374.

Bennett, R. A., B. P. Wernicke, N. A. Niemi, A. M. Friedrich, and J. L. Davis (2003), Contemporary strain rates in the northern Basin and Range province from GPS data, *Tectonics*, *22*(2), 1008, doi:10.1029/2001TC001355.

Briggs, R. W., S. G. Wesnousky, and G. Blewitt (2000), A geologic and geodetic investigation of the Pyramid Lake and Olinghouse Fault Zones, Northern Walker Lane, Nevada, *Eos Trans. AGU*, *81*(48), Fall Meet. Suppl., Abstract T22A-09.

Caskey, J. S., J. W. Bell, B. D. Slemmons, and A. R. Ramelli (2000), Historical surface faulting and paleoseismology of the central Nevada seismic belt, in *Geological Society of America Field Guide 2*, edited by D. R. Lageson, S. G. Peters, and M. M. Lahren, pp. 23–44, Geol. Soc. of Am., Boulder, Colo.

Coblentz, D. D., R. M. Richardson, and M. Sandiford (1994), On the gravitational potential of the Earth's lithosphere, *Tectonics*, *13*(4), 929–945.

Dixon, T. H., S. Robaudo, J. Lee, and M. C. Reheis (1995), Constraints on present-day Basin and Range deformation from space geodesy, *Tectonics*, *14*(4), 755–772.

Dixon, T. H., M. Miller, F. Farina, H. Wang, and D. Johnson (2000), Present-day motion of the Sierra Nevada block and some tectonic implications for the Basin and Range province, North American Cordillera, *Tectonics*, *19*(1), 1–24.

Dong, D., T. A. Herring, and R. W. King (1998), Estimating regional deformation from a combination of space and terrestrial geodetic data, *J. Geod.*, *72*, 200–214.

Doser, D. I. (1986), Earthquake processes in the Rainbow Mountain-Fairview Peak-Dixie Valley, Nevada, Region 1954–1959, *J. Geophys. Res.*, *91*(B12), 12,572–12,586.

Dueker, K. G. (1998), New velocity image of the western U.S. upper mantle: Is heat input from below the lithosphere required?, *Eos Trans. AGU*, *79*(45), Fall Meet. Suppl., F559.

England, P., and D. McKenzie (1982), A thin viscous sheet model for continental deformation, *Geophys. J. R. Astron. Soc.*, *70*, 295–321.

England, P., and P. Molnar (1997), Active deformation of Asia from kinematics to dynamics, *Science*, *278*, 647–650.

Flesch, L. M., W. E. Holt, J. A. Haines, and S.-T. Bingming (2000), Dynamics of the Pacific-North America Plate boundary in the western United States, *Science*, *287*, 834–836.

Flesch, L. M., J. A. Haines, and W. E. Holt (2001), Dynamics of the India-European collision zone, *J. Geophys. Res.*, *10*(B8), 16,435–16,460.

Frank, F. C. (1972), Plate tectonics, the analogy with glacier flow and isostasy, in *Flow and Fracture of Rocks*, *Geophys. Monogr. Ser.*, vol. 16, edited by H. C. Heard, pp. 285–292, AGU, Washington, D. C.

Freund, L. B., and D. M. Barnett (1976), A two-dimensional analysis of surface deformation due to dip-slip faulting, *Bull. Seismol. Soc. Am.*, *66*(3), 667–675.

Grand, S. P. (1994), Mantle shear structure beneath the Americas and surrounding oceans, *J. Geophys. Res.*, *99*(B6), 11,591–11,621.

Hamilton, W. (1978), Mesozoic tectonics of the western United States, in *Mesozoic Paleogeography of the Western United States, Pacific Coast Paleogeography Symposium 2*, edited by D. G. Howell and K. A. McDougall, pp. 33–70, Pac. Sect., Soc. of Econ. Paleontol. and Mineral., Bakersfield, Calif.

Hearn, T. M. (1996), Anisotropic Pn tomography in the western United States, *J. Geophys. Res.*, *101*(B4), 8403–8414.

Hetland, E. A., and B. H. Hager (2003), Postseismic relaxation across the Central Nevada Seismic Belt, *J. Geophys. Res.*, *108*(B8), 2394, doi:10.1029/2002JB002257.

Hodgkinson, K. M., R. S. Stein, and G. Marshall (1996), Geometry of the 1954 Fairview Peak-Dixie Valley earthquake sequence from a joint inversion of leveling and triangulation data, *J. Geophys. Res.*, *101*(B11), 25,437–25,457.

Humphreys, E. D., and K. G. Dueker (1994), Western U.S. upper mantle structure, *J. Geophys. Res.*, *99*(B5), 9615–9634.

Jones, C. H., J. R. Unruh, and L. J. Sonder (1996), The role of gravitational potential energy in active deformation in the southwestern United States, *Nature*, *381*, 37–41.

Lachenbruch, A. H. and J. H. Sass (1978), Models of extending lithosphere and heat flow in the Basin and Range province, in *Cenozoic Tectonics and Regional Geophysics of the Western Cordillera*, edited by R. B. Smith and G. P. Eaton, *Mem. Geol. Soc. Am.*, *152*, 209–250.

Langbein, J., and H. Johnson (1997), Correlated errors in geodetic time series: Implications for time-dependent deformation, *J. Geophys. Res.*, *102*(B1), 591–604.

Larson, K. M., and T. van Dam (2000), Measuring postglacial rebound with GPS and absolute gravity, *Geophys. Res. Lett.*, *27*(23), 3925–3928.

Martinez, L. J., C. M. Meertens, and R. B. Smith (1998), Rapid deformation rates along the Wasatch fault zone, Utah, from first GPS measurements with implications for earthquake hazard, *Geophys. Res. Lett.*, *25*, 567–570.

Minster, J. B., and T. H. Jordan (1984), Vector constraints on Quaternary deformation of the western United States east and west of the San Andreas fault, *Eos Trans. AGU*, *65*(16), 195.

Minster, J. B., and T. H. Jordan (1987), Vector constraints on Western U.S. deformation from space geodesy, neotectonics, and plate tectonics, *J. Geophys. Res.*, *92*(B6), 4798–4804.

Morgan, P., and W. D. Gosnold (1989), Heat flow and thermal regimes in the continental United States, in *Geophysical Framework of the Continental United States*, edited by L. C. Pakiser and W. D. Mooney, *Mem. Geol. Soc. Am.*, *172*, 493–522.

Niemi, N. A., B. P. Wernicke, A. M. Friedrich, M. Simons, R. A. Bennett, and J. L. Davis (2004), BARGEN continuous GPS data across the eastern Basin and Range province, and implications for faults system dynamics, *Geophys. J. Int.*, in press.

Nishimura, T., and W. Thatcher (2003), Rheology of the lithosphere inferred from postseismic uplift following the 1959 Hebgen Lake earthquake, *J. Geophys. Res.*, *108*(B8), 2389, doi:10.1029/2002JB002191.

Parsons, T. (1995), The Basin and Range Province, in *Continental Rifts: Evolution, Structure and Tectonics*, edited by K. Olsen, pp. 277–324, Elsevier Sci., New York.

Ricard, Y., L. Fleitout, and C. Froidevaux (1984), Geoid heights and lithospheric stresses for a dynamic Earth, *Ann. Geophys.*, *2*(3), 267–286.

Savage, J. C., and R. O. Burford (1973), Geodetic determination of relative plate motion in central California, *J. Geophys. Res.*, *78*(B5), 832–845.

Savage, J. C., J. Lisowski, J. L. Svarc, and W. K. Gross (1995), Strain accumulation across the central Nevada seismic zone, 1973–1994, *J. Geophys. Res.*, *100*, 20,257–20,269.

Savage, J. C., W. Gan, and J. L. Svarc (2001), Strain accumulation and rotation in the Eastern California Shear Zone, *J. Geophys. Res.*, *106*(B10), 21,995–22,007.

Smith, D. A., and D. R. Roman (2001), GEOID99 and G99SSS: 1-arc-minute geoid models for the United States, *J. Geod.*, *75*, 469–490.

Sonder, L. J., and C. H. Jones (1999), Western United States Extension: How the west was widened, *Annu. Rev. Earth Planet. Sci.*, *27*, 417–462.

Svarc, J. L., J. C. Savage, W. H. Prescott, and A. R. Ramelli (2002), Strain accumulation and rotation in western Nevada, 1993–2000, *J. Geophys. Res.*, *107*(B5), 2090, doi:10.1029/2001JB000579.

Thatcher, W. (2003), GPS constraints on the kinematics of continental deformation, *Int. Geol. Rev.*, *45*, 191–212.

Thatcher, W., and D. P. Hill (1991), Fault orientations in extensional and conjugate strike-slip environments and their implications, *Geology*, *19*, 1116–1120.

Thatcher, W., G. R. Foulger, B. R. Julian, J. L. Svarc, E. Quilty, and G. W. Bawden (1999), Present-day deformation across the Basin and Range province, western United States, *Science*, *283*, 1714–1718.

Turcotte, D. L. and G. Schubert (1982), *Geodynamics Applications of Continuum Physics to Geological Problems*, John Wiley, Hoboken, N. J.

van der Lee, S., and G. Nolet (1997), Upper mantle S velocity structure of North America, *J. Geophys. Res.*, *102*(B10), 22,815–22,838.

Wallace, R. E. (1978), Geometry and rates of change of fault-generated range fronts, north-central Nevada, *J. Res. U.S. Geol. Surv.*, *6*(5), 637–650.

Wallace, R. E. (1984), Patterns and timing of late quaternary faulting in the Great Basin province and relation to some regional tectonic features, *J. Geophys. Res.*, *89*(B7), 5763–5769.

Webb, F. H. and J. F. Zumberge (1995), An introduction to GIPSY/OASIS-II, *JPL D-11088*, Jet Propul Lab., Pasadena, Calif.

Wernicke, B. P., A. M. Friedrich, N. A. Niemi, R. A. Bennett, and J. L. Davis (2000), Dynamics of plate boundary fault systems from Basin and Range Geodetic Network (BARGEN) and geologic data, *GSA Today*, *10*(11), 1–7.

Williams, S. P. D., Y. Bock, P. Fang, P. Jamason, R. M. Nikolaidis, and L. Prawirodirdjo (2004), Error analysis of continuous GPS position time series, *J. Geophys. Res.*, *109*(B3), B03412, doi:10.1029/2003JB002741.

Zoback, M. L., R. E. Anderson, and G. A. Thompson (1981), Cainozoic evolution of the state of stress and style of tectonism of the Basin and Range province of the western United States, *Philos. Trans. R. Astron. Soc.*, *300*, 407–434.

Zumberge, J. F., M. B. Heflin, D. C. Jefferson, M. M. Watkins, and F. H. Webb (1997), Precise point positioning for the efficient and robust analysis of GPS data from large networks, *J. Geophys. Res.*, *102*(B3), 5005–5017.

W. C. Hammond, Nevada Bureau of Mines and Geology, University of Nevada, Reno, Reno, NV 89557-0088, USA. (whammond@unr.edu)

W. Thatcher, Earthquake Hazards Team, U.S. Geological Survey, 345 Middlefield Road, MS/977, Menlo Park, CA 94025, USA. (thatcher@usgs.gov)